THE JOURNAL OF
PHYSICAL CHEMISTRY C

Article

pubs.acs.org/JPCC

Experimental and Theoretical Evidence for the Reactivity of Bound Intermediates in Ketonization of Carboxylic Acids and Consequences of Acid–Base Properties of Oxide Catalysts

Shuai Wang and Enrique Iglesia*

Department of Chemical and Biomolecular Engineering, University of California at Berkeley, Berkeley, California 94720, United States

Ⓢ *Supporting Information*

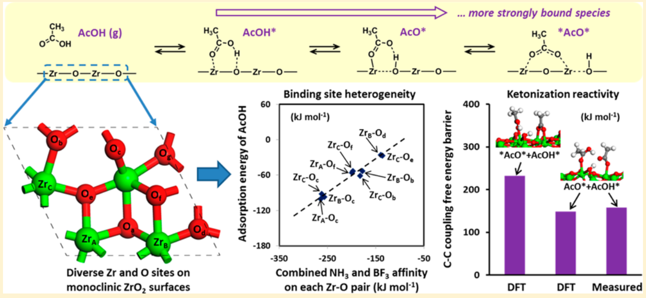

ABSTRACT: Ketonization of carboxylic acids on metal oxides enables oxygen removal and the formation of new C–C bonds for increasing the energy density and chemical value of biomass-derived streams. Information about the surface coverages and reactivity of various bound species derived from acid reactants and the kinetic relevance of the elementary steps that activate reactants, form C–C bonds, and remove O atoms and how they depend on acid–base properties of surfaces and molecular properties of reactants is required to extend the range of ketonization catalytic practice. Here, we examine such matters for ketonization of C_2–C_4 carboxylic acids on monoclinic and tetragonal ZrO_2 (ZrO_2(m), ZrO_2(t)) materials that are among the most active and widely used ketonization catalysts by combining kinetic, isotopic, spectroscopic, and theoretical methods. Ketonization turnovers require Zr–O acid–base pairs, and rates, normalized by the number of active sites determined by titration methods during catalysis, are slightly higher on ZrO_2(m) than ZrO_2(t), but exhibit similar kinetic dependence and the essential absence of isotope effects. These rates and isotope effects are consistent with surfaces nearly saturated with acid-derived species and with kinetically limited C–C bond formation steps involving 1-hydroxy enolates formed via α-C–H cleavage in bound carboxylates and coadsorbed acids; these mechanistic conclusions, but not the magnitude of the rate parameters, are similar to those on anatase TiO_2 (TiO_2(a)). The forms of bound carboxylic acids at Zr–O pairs become more stable and evolve from molecular acids to dissociated carboxylates as the combined acid and base strength of the Zr and O centers at each type of site pair increases; these binding properties are estimated from DFT-derived NH_3 and BF_3 affinities. Infrared spectra during ketonization catalysis show that molecularly bound acids and monodentate and bidentate carboxylates coexist on ZrO_2(m) because of diversity of Zr–O site pairs that prevails on such surfaces, distinct in coordination and consequently in acid and base strengths, and that monodentate and bidentate carboxylates are the most abundant species on saturated ZrO_2 surfaces, consistent with their DFT-derived binding strengths. Theoretical assessments of free energies along the reaction coordinate show that monodentate carboxylates act as precursors to reactive 1-hydroxy enolate intermediates, while strongly bound bidentate carboxylates are unreactive spectators. Higher 1-hydroxy enolate coverages, brought forth by stabilization on the more strongly basic O sites on ZrO_2(m), account for the more reactive nature of ZrO_2(m) than TiO_2(a). These findings indicate that the elementary steps and site requirements for ketonization of C_2–C_4 carboxylic acids are similar on M–O site pairs at TiO_2 and ZrO_2 surfaces, a conclusion that seems general to other metal oxides of comparable acid–base strength.

1. INTRODUCTION

Ketonization forms alkanones with the loss of one C atom from the two carboxylic acid reactants as CO_2 and of three O atoms as equimolar amounts of CO_2 and H_2O.[1,2] These reactions lead to the formation of a new C–C bond and increase the energy density of oxygenates by decreasing their oxygen content.[3−7] Ketonization catalysis occurs over a wide temperature range (473–673 K) on oxides, such as MgO,[8] BaO,[9] MnO_2,[10,11] CeO_2,[12−16] TiO_2,[17−23] and ZrO_2.[4,5,22−28] TiO_2 and ZrO_2 are often reported as the most active, selective, and stable catalysts for such reactions.[3,23]

The elementary steps involved in the ketonization of carboxylic acids on metal oxides involve α-C–H cleavage in bound acids to form 1-hydroxy enolates that subsequently couple with another bound acid molecule to form the new C–C bond. This step is mediated by a transition state (TS) that interacts in a concerted manner with the acid and base centers in metal–oxygen (M–O) site pairs present at oxide surfaces.[2,3,23] These elementary steps are reminiscent of those required for aldol condensation of carbonyl compounds, which also occurs on M–O pairs at TiO_2 and ZrO_2 surfaces;[29−31] condensations, however, form α,β-unsaturated carbonyl products, via facile dehydration of aldol products, while the products

Received: June 19, 2017
Published: July 24, 2017

DOI: 10.1021/acs.jpcc.7b05987
J. Phys. Chem. C 2017, 121, 18030−18046

formed in ketonization C−C coupling steps must eliminate both CO_2 and H_2O to form stable alkanones.[23] Aldol condensation occurs on TiO_2 and ZrO_2 surfaces that remain essentially bare during catalysis, with the consequent formation of enolates via α-H abstraction as the sole kinetically relevant step. Enolates then form a C−C bond via reactions with another carbonyl in fast and kinetically irrelevant subsequent steps.[30,31] In contrast, M−O pairs at oxide surfaces are nearly saturated with adsorbed acids at practical ketonization conditions;[3,20,23] as a result, ketonization turnovers are limited by C−C coupling, instead of 1-hydroxy enolate formation steps. Ketonization rates therefore reflect free energy differences between the C−C coupling TS and the most abundant adsorbed intermediates, as suggested by kinetic, isotopic, and theoretical methods for the specific case of TiO_2 surfaces.[23] These free energy differences depend on the relative stability of these adsorbed precursors and TS structures on M−O pairs, which reflect, in turn, the strength of the acid−base centers in such M−O site pairs. Such properties are inaccessible to direct assessment by experiments; as a result, their consequences for reactivity have remained qualitative and supported by inferences from observed trends between ketonization rates and the binding energies of probe molecules.[2]

The quantitative determination of intrinsic reactivity and activation free energies for ketonization and their benchmarking against theoretical treatments requires the measurement of turnover rates and thus an accurate count of the number of active sites present on oxides under the conditions of the catalytic reaction. Such site counts have been recently measured from the titration of acid−base pairs during catalysis and the number of titrants required for full suppression of reactivity.[30,31] These measurements have allowed rigorous comparisons of ketonization site reactivity on TiO_2 and ZrO_2.[23]

Carboxylic acids bind molecularly on oxides, but also dissociate at one M−O site pair to form monodentate carboxylates or at two vicinal M−O site pairs to form the bidentate analogues.[2,3,23] The stability and reactivity of these acid-derived species determine their relative coverages and their respective contributions to ketonization turnovers. Kinetic, spectroscopic, and theoretical studies[23] show that monodentate carboxylates prevail as the most abundant surface species (MASI) during ketonization turnovers and act as reactive intermediates on anatase TiO_2 (TiO_2(a)). Bidentate carboxylates, often proposed as the active ketonization intermediates,[2,3] are unreactive spectators, typically present at low coverages on TiO_2(a) surfaces. The weaker basic O atoms in rutile TiO_2 (TiO_2(r)) relative to TiO_2(a) preclude dissociation, leading to bound molecular acids as ketonization intermediates, while the short Ti−Ti distances in TiO_2(r) (relative to those in TiO_2(a)) favor strongly bound bidentate carboxylates, which act as unreactive spectators and preclude the formation of active monodentate species.[23] Such stability, prevalence, and reactivity of these types of bound acids remain unexplored and uncertain on ZrO_2, the ketonization catalyst most often used in practice.[3,23,24]

Here, kinetic and isotopic data are combined with *in situ* infrared spectra and theoretical methods to examine the mechanism of ketonization reactions of C_2−C_4 carboxylic acids on monoclinic and tetragonal ZrO_2 (ZrO_2(m), ZrO_2(t)) at the near saturation coverages prevalent during catalysis. The conclusions of this study are compared with those of recent studies on TiO_2 surfaces[23] to illustrate the broad and more general implications of the proposed elementary steps and site requirements to ketonization catalysis on metal oxides.

C−C bond formation via 1-hydroxy enolate reactions with a vicinal bound acid is the sole kinetically relevant step for C_2−C_4 acids on ZrO_2(m) and ZrO_2(t). The Zr and O centers on ZrO_2(m) exhibit diverse coordinations and acid−base properties, probed here through DFT-derived binding energies for NH_3 and BF_3 molecules. Acids bind more strongly, and the prevalent bound species evolve from molecular to dissociated forms as the combined NH_3 and BF_3 affinities for Zr and O centers increase with a decrease in their coordination. Infrared spectra during ketonization catalysis show that bound ethanoic acid molecules (AcOH*) and monodentate and bidentate carboxylates (AcO*, *AcO*) coexist on ZrO_2(m), and that these ZrO_2(m) surfaces are nearly saturated with the two carboxylates. Theoretical treatments of proposed ketonization elementary steps discern that AcO* and AcOH* are the reactive intermediates involved in ketonization turnovers on ZrO_2(m), while *AcO* species are unreactive because of their strong binding at Zr−O site pairs. These theoretical treatments also indicate that O atoms that act as stronger basic centers account for the higher ketonization reactivity of ZrO_2(m) over TiO_2(a), because they lead to more stable 1-hydroxy enolates and thus lower activation barriers for the kinetically relevant C−C bond formation. The quantitative benchmarking of theory with kinetic and spectroscopic data provides the mechanistic connections required for accurate descriptors of reactivity for C−C bond formation reactions on oxides and for the consequences of acid−base properties of the M−O site pairs that mediate such reactions.

2. METHODS

2.1. Catalyst Synthesis and Characterization.

The detailed synthesis and characterization protocols for monoclinic ZrO_2 (ZrO_2(m)) and tetragonal ZrO_2 (ZrO_2(t)) have been reported previously[23] and are therefore described only briefly below.

ZrO_2(m) was synthesized by treating an aqueous solution of $ZrO(NO_3)_2$ ($ZrO(NO_3)_2{\cdot}2H_2O$, 99.5%, Sigma-Aldrich) and urea ($CO(NH_2)_2$, 99%, Aldrich) within a Teflon-lined stainless-steel autoclave at 433 K for 20 h.[32] The precipitates were rinsed with deionized water until the filtrate reached a pH of 7−8; the sample was then exposed to ambient air at 383 K overnight using a convection oven and then heated in flowing dry air ($1.67\ cm^3\ g^{-1}\ s^{-1}$, 99.999%, Praxair) from ambient temperature to 673 K (at $0.167\ K\ s^{-1}$) and held for 4 h.

ZrO_2(t) was prepared by treating an aqueous solution of $ZrOCl_2$ ($ZrOCl_2{\cdot}8H_2O$, 99.5%, Sigma-Aldrich) in a round-bottom flask at a pH of 10 set by the addition of 5.0 M NH_4OH (99.99%, Sigma-Aldrich) at 333 K for 4 h.[33] The resulting solids were rinsed with deionized water until the filtrates were neutral (pH 7−8) and free of Cl^- ions examined by 0.2 mmol cm^{-3} aqueous $AgNO_3$ (>99.0%, Sigma-Aldrich) solution, and then thermally treated as in the case of ZrO_2(m).

Cu/SiO_2 catalysts (~20% wt Cu), used here together with H_2 in order to inhibit ZrO_2 deactivation during ketonization,[23] were synthesized by homogeneous deposition−precipitation methods previously reported.[30] An aqueous suspension of colloidal silica (30 wt %, LUDOX SM-30), $Cu(NO_3)_2$ ($Cu(NO_3)_2{\cdot}2.5H_2O$, 99.99%, Sigma-Aldrich), and urea ($CO(NH_2)_2$, 99%, Aldrich) were treated at 363 K for 20 h; the filtered solids were washed with deionized water until the rinse solution gave a pH of 7−8, and then treated sequentially in a

DOI: 10.1021/acs.jpcc.7b05987
J. Phys. Chem. C 2017, 121, 18030−18046

convection oven at 383 K overnight, in flowing dry air (1.67 $cm^3\ g^{-1}\ s^{-1}$, 99.999%, Praxair) at 723 K (from ambient temperature to 723 at 0.167 $K\ s^{-1}$) for 5 h, and in flowing 10% H_2/He (5.56 $cm^3\ g^{-1}\ s^{-1}$, 99.999%, Praxair) at 573 K (from ambient to 573 at 0.033 $K\ s^{-1}$) for 2 h.

Crystalline phases of all samples were identified by powder X-ray diffraction measurements (Cu Kα radiation, λ = 0.15418 nm, 40 kV, 40 mA, Bruker D8 Advance).[23,30] Exposed acid−base pairs on ZrO_2(m) and ZrO_2(t), relevant to both aldol condensation of carbonyl compound and ketonization of carboxylic acid on these oxides,[23] were counted from the amount of propanoic acid titrants (C_2H_5COOH, >99.5%, Sigma-Aldrich; 20 Pa) required to fully suppress aldol condensation rates of acetone (CH_3COCH_3, >99%, Fisher; 0.8 kPa) at 453 K. These measured acid−base pair densities for ZrO_2(m) (6.0 nm^{-2}) and ZrO_2(t) (5.8 nm^{-2}) were used to report ketonization rates as turnover rates and calculate ketonization free energy barriers.[23,30,31]

2.2. Measurements of Carboxylic Acid Ketonization Rates. ZrO_2 samples and 20% wt Cu/SiO_2 cocatalysts were mixed using a mortar and pestle (ZrO_2/(Cu/SiO_2) = 1/1 mass), and were then pressed into wafers, crushed, and sieved to retain 125−180 μm aggregates. These physical mixtures were loaded within an isothermal packed-bed reactor (1.0 cm i.d.) with plug-flow hydrodynamics and heated in flowing 10% H_2/He (5.56 $cm^3\ g^{-1}\ s^{-1}$, 99.999%, Praxair) from ambient temperature to 543 at 0.0833 $K\ s^{-1}$ and held at 543 K for 2 h before cooling to the desired reaction temperature (503−533 K).

Carboxylic acids (ethanoic acid (CH_3COOH, >99.7%, Sigma-Aldrich), propanoic acid (C_2H_5COOH, >99.5%, Sigma-Aldrich), and butanoic acid (C_3H_7COOH, >99%, Sigma-Aldrich)) were introduced as liquids using a syringe pump (Cole Parmer, 74900 series) and vaporized into H_2 and He flows metered by electronic mass flow controllers (Porter, Inc.). The liquid and gas flow rates were controlled to achieve the desired acid and H_2 pressures (0.2−3.0 and 20 kPa, respectively) and to set reactor residence times that kept the conversions of acid reactants below 15%. Transfer lines were maintained above 430 K in order to avoid reactant and product condensation. Isotopic effects on ketonization rates for ethanoic acid were examined by using ethanoic acid-d_4 (CD_3COOD, >99%, Sigma-Aldrich) and D_2 (>99%, Praxair) as reactants, instead of the respective species in their protium forms.

The components in effluent streams were identified using known standards and mass spectrometry (HP 5972 mass spectrometer). Their concentrations were measured by gas chromatography (Agilent 6890) using a capillary column (Agilent, HP-1, methyl silicone, 50 m, 0.32 mm ID × 1.05 μm) and a flame ionization detector for carboxylic acids, alkanones, and other oxygenates, and using a packed column (Porapak-Q, 4.8 m, 80−100 mesh) and a thermal conductivity detector for H_2, H_2O, and CO_2. Conversions and selectivities were calculated on a carbon basis. Ketonization rates were corrected for mild deactivation[23] by periodic rate measurements at a reference condition (1.0 kPa acid reactant, 20 kPa H_2, 523 K). These rates are reported as the number of acid molecules converted per ks divided by the number of exposed Zr−O pairs measured by the methods described above (Section 2.1).

2.3. Infrared Spectroscopy Measurements. Species bound on ZrO_2(m) during ethanoic acid ketonization at 523 K were detected by infrared spectra using a Nicolet 8700 FT-IR spectrometer with a Hg−Cd−Te (MCT) detector. Self-supporting ZrO_2 wafers (2−5 mg cm^{-2}) were sealed within a cell equipped with KBr windows and treated in flowing He (5.56 $cm^3\ g^{-1}\ s^{-1}$, 99.999%, Praxair) by heating from ambient temperature to 573 K (0.0833 $K\ s^{-1}$), holding at 573 K for 2 h, and cooling to 523 K. Liquid ethanoic acid (>99.7%, Sigma-Aldrich) was then introduced into the He flow by a syringe pump at molar rates required to achieve the desired acid pressure (0.2−1.6 kPa). Spectra were collected in the 4000−650 cm^{-1} range with 2 cm^{-1} resolution by averaging 64 scans.

2.4. Density Functional Theory Methods. Periodic plane-wave density functional theory (DFT) was used to address the energetics of the elementary steps involved in ethanoic acid ketonization on ZrO_2(m) surfaces. All DFT calculations were carried out using the Vienna ab initio simulation package (VASP)[34−37] with projector augmented-wave (PAW) pseudopotentials to describe electron−core interactions for all atoms (energy cutoff: 400 eV).[38,39] The Perdew−Burke−Ernzerhof (PBE) functional was used within the generalized-gradient approximation (GGA)[40,41] to describe exchange and correlation interactions among electrons. Grimme's D3BJ dispersion corrections[42,43] were used at each energy minimization iteration to account for van der Waals interactions.

The (−111) plane, the most stable surface in ZrO_2(m) crystals,[24] was used to simulate bound species and ketonization elementary steps. Periodic (−111) slabs of a unit cell (containing three Zr atoms and seven O atoms on their outermost surfaces) were constructed from DFT-derived ZrO_2(m) bulk structures ($P2_1/c$, a = 0.522 nm, b = 0.528 nm, c = 0.539 nm).[31] Each unit cell contained four Zr_4O_8 layers and a vacuum layer of 1.5 nm along the z-direction. The three Zr_4O_8 layers closest to the surface were relaxed in all energy minimization steps, while the bottom layer was held at the position in its bulk structure. Energies and forces were calculated using a 4 × 4 × 1 Monkhorst-pack sampling k-point set[44] with respective energy and force convergence criteria of 1×10^{-6} eV and of 0.05 eV $Å^{-1}$ on each unconstrained atom. Dipole and quadrupole corrections[45] were used during each optimization step in order to remove any artifactual interactions among periodic images along the z-direction caused by dipoles in vicinal images.

Transition state (TS) structures were first isolated using the nudged elastic band (NEB) method[46,47] with 8−12 images along the reaction coordinate between reactant and product states. Structures with the highest energy along NEB-optimized paths were then taken as the starting point for refining the TS search using the Dimer algorithm.[48] A single Γ-centered k-point and a convergence criteria of 1×10^{-4} eV (for electronic energies) and 0.1 eV $Å^{-1}$ (for forces at each unconstrained atom) were used in NEB calculations. Dimer calculations were carried out using the same k-point mesh and the same convergence criteria as for stable bound species.

Vibrational analyses were performed for optimized structures in order to determine their enthalpies, entropies, and Gibbs free energies.[49] Atoms in adsorbed species and at the outermost ZrO_2 layer were allowed to move in frequency calculations, because relaxation of the other layers in the ZrO_2 slab would impose prohibitive computational costs. The contributions to entropies and free energies from low-frequency modes (<60 cm^{-1}) are inaccurate for weakly bound species in periodic VASP models;[50] they were replaced by the rotational modes in their gaseous analogues (multiplied by 0.70), as indicated by measured enthalpies and entropies for adsorption of gaseous molecules on oxides.[51]

The affinity of NH_3 (E_{AA}) for Lewis acid centers (LA) is defined here as the energy released upon binding of a gaseous NH_3 molecule on such centers:

$$E_{AA} = E_{NH_3-LA} - E_{LA} - E_{NH_3} \tag{1}$$

Here, E_{NH_3-LA} is the energy of the NH_3−LA pair, and E_{LA} and E_{NH_3} are those for the noninteracting LA and NH_3(g), respectively. The affinity of BF_3 (E_{BA}) for a Lewis base center (LB) was similarly defined:

$$E_{BA} = E_{BF_3-LB} - E_{LB} - E_{BF_3} \tag{2}$$

with the analogous definitions for E_{BF_3-LB}, E_{LB}, and E_{BF_3}. E_{AA} and E_{BA} represent rigorous descriptors of the strength of the respective acid and base centers in M−O pairs. The E_{AA} and E_{BA} values for the respective Zr and O sites exposed on ZrO_2(m) (−111) surfaces were assessed using a periodic slab model of a unit cell and DFT treatment protocols as described above. Such E_{AA} and E_{BA} values were also calculated for the Ti and O sites exposed on TiO_2(a) (101) surfaces using a periodic slab model of a 1 × 2 supercell that was constructed and reported in detail elsewhere,[23] so as to compare ZrO_2(m) and TiO_2(a) surfaces and to assess the consequences of acid−base properties for ketonization reactivity.

3. RESULTS AND DISCUSSION

3.1. Dependence of Ketonization Rates on the Pressure of Carboxylic Acid Reactants on Monoclinic and Tetragonal ZrO_2. C_2−C_4 carboxylic acids ($C_nH_{2n+1}COOH$, n = 1−3) formed equimolar mixtures of symmetric alkanones ($C_nH_{2n+1}C(=O)C_nH_{2n+1}$), H_2O, and CO_2 with carbon selectivities above 95% (at 0−11% acid conversion, 503−533 K) on both monoclinic and tetragonal ZrO_2 (ZrO_2(m), ZrO_2(t)), as also reported in previous studies.[23] Ketonization turnover rates of ethanoic acid per exposed Zr−O pair (ZrO_2(m) 6.0 nm^{-2}, ZrO_2(t) 5.8 nm^{-2}, Section 2.1) were proportional to acid pressure at low pressures (<0.4 kPa) but then reached nearly constant values at higher acid pressures (>2 kPa, 523 K, Figure 1), as also shown on anatase TiO_2 (TiO_2(a)).[23] These effects of acid pressure on ketonization rates were similar for ethanoic, propanoic, and butanoic acids at all temperatures (503−533 K) and on both ZrO_2(m) (Figure 2) and TiO_2(a);[23] thus, we conclude that the mechanistic features responsible for such a kinetic response are common to all these carboxylic acids and to ZrO_2 and TiO_2 catalysts.

Ketonization turnover rates for perdeuterated ethanoic acid (CD_3COOD) were similar to those for undeuterated reactants (CH_3COOH) on both ZrO_2(m) and ZrO_2(t) (r_H/r_D = 1.1 for both ZrO_2(m) and ZrO_2(t), 0.2−2.2 kPa, 523 K, Figure 1), as also observed on TiO_2(a).[23] These data indicate that the formation of the C−C bond, instead of the H abstraction step required to form 1-hydroxy enolates, limits ketonization turnovers on ZrO_2 surfaces, as is also the case on TiO_2(a). This step involves the reaction between an acid-derived 1-hydroxy enolate, present in equilibrium with the gaseous acid reactant, and a vicinal coadsorbed acid molecule.[23] Ethanoic acid ketonization turnover rates are slightly higher on ZrO_2(m) than ZrO_2(t) (Figure 1), as also shown in previous studies for the reaction of stearic acid on these two crystalline ZrO_2 phases;[4] these ethanoic acid ketonization rates are higher on ZrO_2 than on TiO_2(a) (1.43, 1.15, and 0.26 ks^{-1} on ZrO_2(m), ZrO_2(t), and TiO_2(a), respectively; 523 K, 3.0 kPa ethanoic acid; Figure 1). Such differences in reactivity are likely to reflect differences in the acid−base binding properties and in the distances in metal−oxygen (M−O) site pairs exposed on these different oxide surfaces. Such binding properties and M−O distances are discussed next as descriptors of reactivity in the context of the elementary steps involved and their kinetic relevance (Section 3.2) and of the binding properties of ZrO_2 surfaces based on DFT estimates of the interaction energies of probe molecules (Section 3.3).

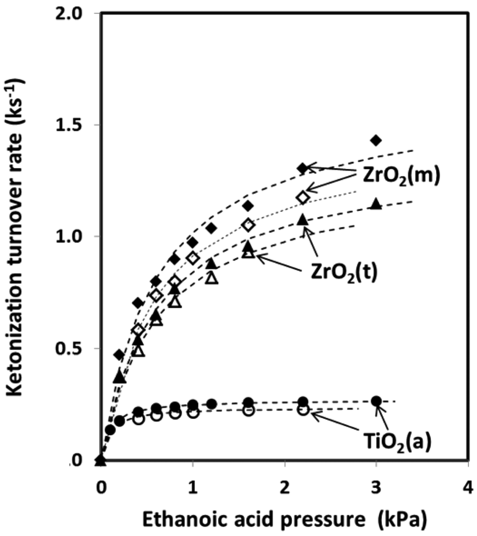

Figure 1. Effects of ethanoic acid pressure on ketonization turnover rates catalyzed by ZrO_2 and TiO_2 (oxide + 20% wt Cu/SiO_2 (1:1 mass), 523 K, CH_3COOH and 20 kPa H_2 for ZrO_2(m) (♦), ZrO_2(t) (▲), and TiO_2(a) (●), CD_3COOD and 20 kPa D_2 for ZrO_2(m) (◊), ZrO_2(t) (Δ), and TiO_2(a) (○)). Dashed lines represent the regressed fits to the mechanism-based functional form of eq 3. Turnover rates on TiO_2(a) are adapted from ref 23.

3.2. Elementary Steps of Ketonization and Their Kinetic Relevance on ZrO_2 and TiO_2. Ketonization rates are accurately described by Langmuirian treatments of elementary steps occurring at vicinal M−O pairs on TiO_2[23] and ZrO_2 (shown below), as depicted in Scheme 1 for ethanoic acid (AcOH) and vicinal Zr−O pairs on ZrO_2(m) surfaces. These surfaces, in contrast with TiO_2 surfaces, exhibit significant diversity in structure and properties.[24,31] In Section 3.3, the combined DFT-derived NH_3 and BF_3 affinity values (eqs 1 and 2) at the M and O centers in Zr−O site pairs with different coordination are shown to describe the binding energy of the acid reactants. As these combined affinities increase, the predominant configuration of the bound acids evolves from the molecular form to carboxylates, and their binding at the Zr−O pair becomes stronger. Here, Zr_I−O_I and Zr_{II}−O_{II} denote the two vicinal Zr−O pairs (Scheme 1) required to complete AcOH ketonization turnovers on ZrO_2(m). Zr_I−O_I is the Zr−O pair with the highest NH_3 and BF_3 combined affinity on ZrO_2(m).

The reactivity data and theoretical treatments below indicate that the O−H bond in AcOH dissociates at Zr_I−O_I pairs to form a H atom at the O_I site and a monodentate carboxylate (AcO*) at the Zr_I center; in such structures, AcO* is stabilized by H-bonding interactions with the H atom abstracted from AcOH (step 1, Scheme 1). In contrast, AcOH remains in its molecular form (AcOH*) at the Zr_{II}−O_{II} pair, with its carbonyl

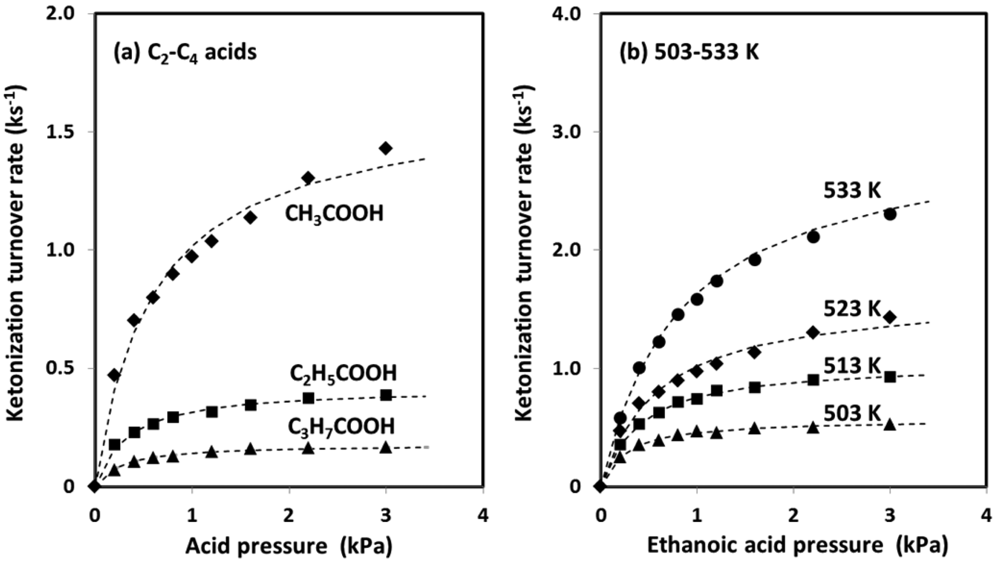

Figure 2. Effects of reactant pressure on ketonization rates for (a) C_2−C_4 carboxylic acids at 523 K and for (b) ethanoic acid at 503−533 K (ZrO_2(m) + 20% wt Cu/SiO_2 (1:1 mass), 20 kPa H_2). Dashed lines represent the regressed fits to the mechanism-based functional form of eq 3.

O atom interacting with the Zr_{II} center and its acidic H atom with the O_{II} site (step 2, Scheme 1).

The cleavage of the α-C−H bond in adsorbed AcO* at the Zr_I−O_I pair forms a proton at the O_I site and a 1-hydroxy enolate at the Zr_I center (step 3, Scheme 1). Such 1-hydroxy enolates carry out a nucleophilic attack at coadsorbed AcOH* species bound at the neighboring Zr_{II}−O_{II} pair on ZrO_2(m) to form a new C−C bond (step 4, Scheme 1). This step forms an unstable α-hydroxy γ-carboxy alkoxide, which sequentially eliminates H_2O and CO_2 (steps 5−8, Scheme 1) to give the surface enolate precursor to the final alkanone product, which forms via the reattachment of the proton previously abstracted from AcO* in forming the 1-hydroxy enolate (step 9, Scheme 1) and then desorbs as the gaseous alkanone (step 10, Scheme 1) to complete a catalytic ketonization turnover.

In addition to the formation of AcO* and AcOH*, AcOH molecules can also dissociate on vicinal Zr═O pairs to form bidentate carboxylates (*AcO*). Such species interact with the two Zr centers through each of the two O atoms in *AcO* and the cleaved H atom bound at one of the lattice O atoms (step 11, Scheme 1). These bidentate carboxylates have been previously considered as the reactive ketonization intermediates, instead of their monodentate analogues.[11−22,24−26] On TiO_2(a), kinetic, infrared, and theoretical methods recently showed that bidentate carboxylates act as unreactive spectators that merely block active M−O site pairs,[23] as we show here also on ZrO_2(m) (Section 3.5). These strongly bound bidentate carboxylates exist in quasiequilibrium with traces of gaseous ketene ($H_2C{=}C{=}O$) and H_2O formed via dehydration of *AcO* on TiO_2(a).[23] The presence of H_2 and a hydrogenation function, such as dispersed Cu metal particles, at locations within diffusion distances from Ti═O pairs allows the continuous scavenging of ketene to acetaldehyde as a mechanism for the removal of unreactive bidentate carboxylates from TiO_2 surfaces; in doing so, such strategies render TiO_2(a) catalysts stable during ketonization catalysis.[23] The desorption of ketene from ZrO_2(m), however, is slower than that from TiO_2(a),[23] consistent with its stronger binding, making such scavenging less effective and, in contrast with TiO_2(a), leading to very slow but detectable deactivation during ketonization on ZrO_2.

The similar kinetic rate dependence on acid pressure and the weak kinetic H/D isotope effects on ZrO_2(m) and TiO_2(a) (Figure 1) indicate that 1-hydroxy enolate reactions with coadsorbed acids (step 4, Scheme 1) limit ketonization rates on both catalysts, as shown earlier on TiO_2(a)[23] and below on ZrO_2. Such a limiting step in Scheme 1, taken together with Zr_I−O_I pairs saturated by monodentate carboxylates, with the quasiequilibrated nature of steps 2 and 3, and with the lack of inhibition by ketonization products (Figure S1 of Supporting Information (SI)), leads to the rate equation:

$$\frac{r}{[L]} = \frac{\overrightarrow{k_4} K_2 K_3 P_{\mathrm{acid}}}{1 + K_2 P_{\mathrm{acid}}} \tag{3}$$

Here, $[L]$ is the number of active Zr−O site pairs, and P_{acid} is the acid pressure; $\overrightarrow{k_x}$ and K_x denote the forward rate constant and equilibrium constant, respectively, for each step x in Scheme 1.

Ketonization rates for all C_2−C_4 acids on ZrO_2(m) are accurately described by eq 3 (Figure 2; regressed parameters in Table 1). Measured $(\overrightarrow{k_4}K_3)_H/(\overrightarrow{k_4}K_3)_D$ and $(K_2)_H/(K_2)_D$ isotopic ratios on ZrO_2(m) are 1.2 ± 0.1 and 1.0 ± 0.1, respectively (523 K), in agreement with the kinetic relevance of the C−C bond formation step (step 4, Scheme 1). These weak H/D isotope effects indicate that α-C−H bond cleavage in AcO* is equilibrated at Zr_I−O_I pairs (step 3, Scheme 1), as is also the case for molecular adsorption of AcOH at Zr_{II}−O_{II} pairs (step 2, Scheme 1). A kinetically relevant H abstraction step that forms 1-hydroxy enolates would lead to much larger isotope effects, such as those observed in aldol condensation reactions that are limited by enolate formation via α-H abstraction (k_H/k_D = 2.4).[30]

The K_2 term in eq 3 reflects the free energy for molecular adsorption of carboxylic acids at the Zr_{II}−O_{II} pair ($\Delta G_{\mathrm{AcOH}*}$) (Scheme 2):

$$K_2 = \exp(-\Delta G_{\mathrm{AcOH}*}/RT) \tag{4}$$

Scheme 1. Proposed Elementary Steps for Carboxylic Acid Ketonization on ZrO_2(m) Surfaces with Asymmetric Acid–Base Zr–O Site Pairs[a]

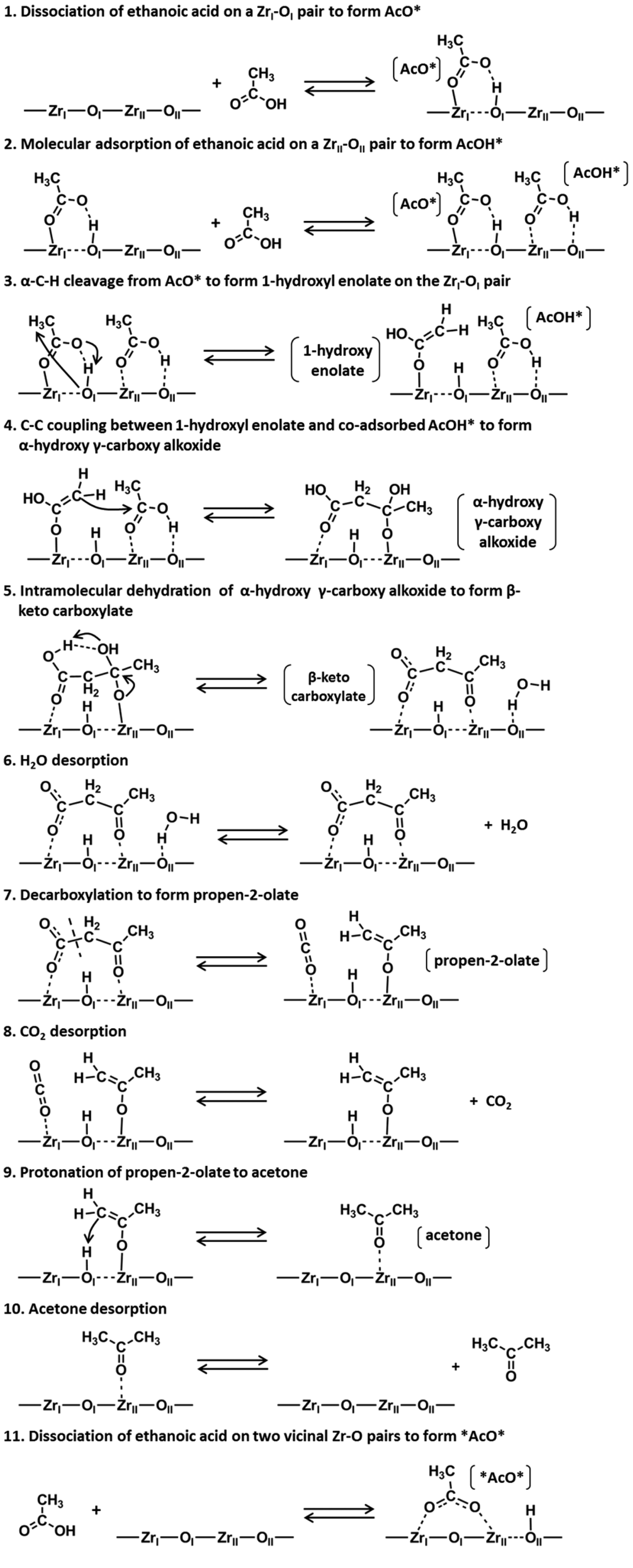

[a] Zr_I–O_I–Zr_{II}–O_{II} sites represent a catalytically relevant domain prevalently exposed on ZrO_2(m), in which the Zr_I–O_I pair has the highest combined NH_3 and BF_3 affinity among all Zr–O pairs on ZrO_2(m). Shown for ethanoic acid as the illustrative example.

Scheme 2 shows that ΔG_{AcOH*} is given by

$$\Delta G_{AcOH*} = G_{AcO*+AcOH*} - G_{AcO*} - G_{acid} \tag{5}$$

Here, $G_{AcO*+AcOH*}$ is the sum of the free energies for a monodentate carboxylate and a vicinal molecular acid bound at Zr_I–O_I–Zr_{II}–O_{II} sites, while G_{AcO*} and G_{acid} are the respective free energies for an isolated monodentate carboxylate at Zr_I–O_I–Zr_{II}–O_{II} sites and the gaseous carboxylic acid.

The measured ΔG_{AcOH*} value on ZrO_2(m) is −22 ± 1 kJ mol^{-1} (523 K, Table 1), and its enthalpy and entropy components (ΔH_{AcOH*}, ΔS_{AcOH*}), determined from the effects of temperature on ΔG_{AcOH*} (503–533 K, Figure 3a), are −89 ± 4 kJ mol^{-1} and −127 ± 7 J mol^{-1} K^{-1}, respectively. These ΔG_{AcOH*} values reflect the adsorption of AcOH at the Zr_{II}-O_{II} pairs according to Scheme 2. Such ΔG_{AcOH*} values become more negative as the alkyl chain length of the acid reactant increases (−22 ± 1 kJ mol^{-1} for ethanoic acid; −26 ± 2 kJ mol^{-1} for butanoic acid; 523 K, Table 2), as expected from the more effective van der Waals contacts between the larger acid molecules and the oxide surfaces.

The $\overrightarrow{k_4}K_3$ term in eq 3 determines the maximum attainable ketonization turnover rates, which occur when AcOH* species reach saturation coverages ($K_2P_{acid} \gg 1$). This $\overrightarrow{k_4}K_3$ term is determined by the free energy difference ($\Delta G^{\ddagger}_{CC}$) between the C–C bond formation transition states ($G^{\ddagger}_{CC}$, Scheme 2) and their bimolecular AcO*–AcOH* precursors bound at Zr_I–O_I–Zr_{II}–O_{II} sites ($G_{AcO*+AcOH*}$):

$$\overrightarrow{k_4}K_3 = \frac{k_BT}{h}\exp(-\Delta G^{\ddagger}_{CC}/RT) \tag{6}$$

$$\Delta G^{\ddagger}_{CC} = G^{\ddagger}_{CC} - G_{AcO*+AcOH*} \tag{7}$$

Measured $\Delta G^{\ddagger}_{CC}$ values for ZrO_2(m) increased slightly from 158 ± 1 kJ mol^{-1} (ethanoic acid) to 168 ± 1 kJ mol^{-1} (butanoic acid) as the R group in RCOOH varied from H, to CH_3 and C_2H_5 (523 K, Table 1). This trend is expected from steric hindrance at the point of nucleophilic attack, as also found on TiO_2(a) for both ketonization[23] and aldol condensation[31] reactions. For ethanoic acid, $\Delta G^{\ddagger}_{CC}$ values are smaller on ZrO_2(m) (158 ± 1 kJ mol^{-1}, 523 K, Table 1) than on TiO_2(a) (166 ± 1 kJ mol^{-1}),[23] consistent with their differences in turnover rates. The enthalpy component of $\Delta G^{\ddagger}_{CC}$ ($\Delta H^{\ddagger}_{CC}$) is smaller on ZrO_2(m) (117 ± 5 kJ mol^{-1}, Figure 3b) than on TiO_2(a) (137 ± 1 kJ mol^{-1}),[23] while the respective entropy components of $\Delta G^{\ddagger}_{CC}$ ($\Delta S^{\ddagger}_{CC}$) are more negative on ZrO_2(m) (−79 ± 10 kJ mol^{-1} K^{-1} (Figure 3b) vs −56 ± 1 kJ mol^{-1} K^{-1} on TiO_2(a)[23]). Thus, the more reactive nature of ZrO_2(m) reflects more effective enthalpic TS stabilization and more strongly bound (and less mobile) TS structures on ZrO_2(m) than on TiO_2(a).

In what follows, theoretical and spectroscopic methods are used to assess the identity and stability of bound species at acid–base Zr–O site pairs on ZrO_2(m) during ketonization catalysis (Sections 3.3 and 3.4), the kinetic relevance of C–C bond formation steps, and the relative coverages and reactivity of acid-derived bound species (Section 3.5). These inquiries illustrate the mechanistic link between the properties of M–O site pairs, specifically the affinity of their acid and base centers, and their involvement as binding sites for different acid-derived species and for concerted interaction with the TS structures that mediate C–C bond formation (Section 3.6).

DOI: 10.1021/acs.jpcc.7b05987
J. Phys. Chem. C 2017, 121, 18030–18046

Table 1. Measured K_2, $\overrightarrow{k_4}K_3$, ΔG_{AcOH^*}, and $\Delta G^{\ddagger}_{CC}$ Values[a] for Ketonization of C_2−C_4 Carboxylic Acids at 503−533 K on $ZrO_2(m)$[b]

reactant	T (K)	K_2 (kPa^{-1})	ΔG_{AcOH^*} (kJ mol^{-1})	$\overrightarrow{k_4}K_3$ (10^{-3} (Zr−O)$^{-1}$ s^{-1})	$\Delta G^{\ddagger}_{CC}$ (kJ mol^{-1})
CH_3COOH	503	4.0 ± 0.6	−25 ± 1	0.57 ± 0.02	157 ± 1
	513	2.5 ± 0.2	−24 ± 1	1.1 ± 0.1	157 ± 1
	523	1.7 ± 0.5	−22 ± 1	1.6 ± 0.2	158 ± 1
	533	1.2 ± 0.2	−21 ± 1	3.0 ± 0.2	159 ± 1
CD_3COOD	523	1.7 ± 0.5	−22 ± 1	1.5 ± 0.5	159 ± 1
C_2H_5COOH	523	3.1 ± 0.8	−25 ± 2	0.42 ± 0.04	164 ± 1
C_3H_7COOH	523	3.7 ± 1.0	−26 ± 2	0.18 ± 0.01	168 ± 1

[a]From regression of all rate data to the functional form of eq 3. [b]Fitted data adopted from Figures 1 and 2.

Scheme 2. Schematic Reaction Coordinate Diagram for Carboxylic Acid Ketonization on $ZrO_2(m)$[a]

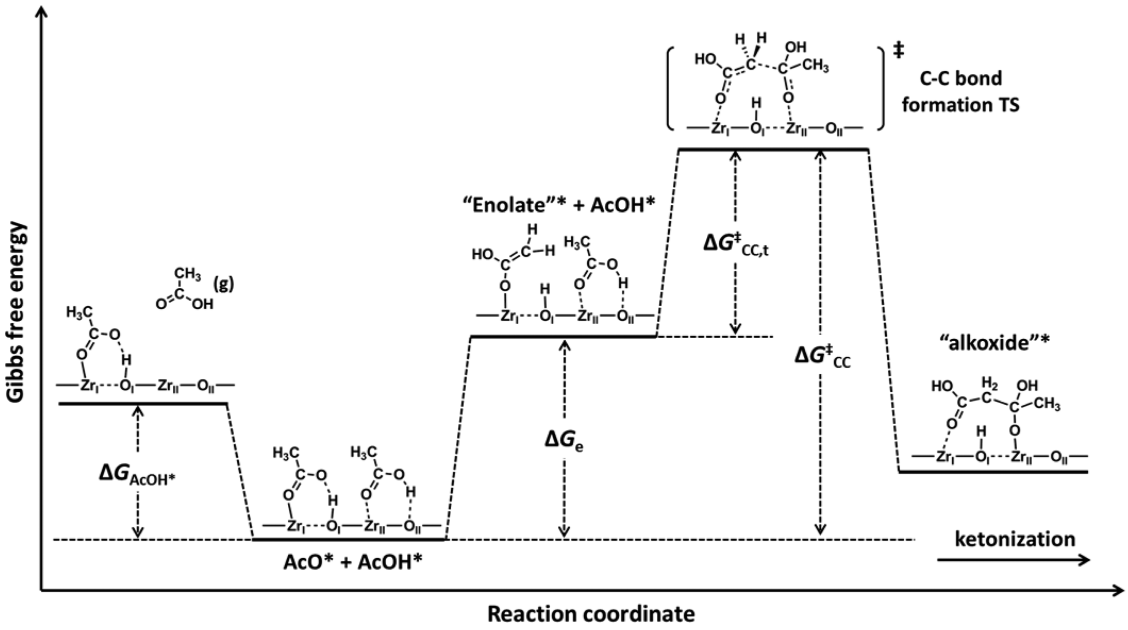

[a]Shown for ethanoic acid as the illustrative example. Asymmetric Zr_I−O_I−Zr_{II}−O_{II} sites represent vicinal Zr−O pairs containing Zr and O sites that differ in acid and base strengths. ΔG_{AcOH^*} is the experimentally accessible free energy change for molecular adsorption of carboxylic acid (eq 4); $\Delta G^{\ddagger}_{CC}$ is the experimentally accessible apparent free energy barrier for the C−C bond formation (eq 6), reflecting the sum of the free energy difference between a bound 1-hydroxy enolate and a monodentate carboxylate (ΔG_e) and the free energy difference between the C−C bond formation transition state and its 1-hydroxy-enolate-acid pair precursor ($\Delta G^{\ddagger}_{CC,t}$).

3.3. Theoretical Assessment of Carboxylic-Acid-Derived Species on Monoclinic ZrO_2 at Catalytic Temperatures.

The (−111) plane is the prevalent and most stable exposed surface on $ZrO_2(m)$.[24] Its structure illustrates the diverse Zr−O site pairs prevalent on $ZrO_2(m)$ surfaces as described below. The outermost $ZrO_2(m)$ (−111) layer contains three Zr atoms per unit cell (Zr_A−Zr_C sites, Scheme 3), each with a lower coordination number (CN) of 6 (Table 2) than in bulk $ZrO_2(m)$ (CN = 7). These centers have DFT-derived NH_3 affinities (E_{AA}, eq 1) ranging from −95 to −102 kJ mol^{-1} (Table 2); this range reflects the distinct O atoms connected to these three Zr centers. The E_{AA} values exponentially averaged over these Zr centers on $ZrO_2(m)$ (−111) (−100 kJ mol^{-1}, Table 2) are less negative than for the single Ti center on $TiO_2(a)$ (101) (−111 kJ mol^{-1}, Table 2); such differences are consistent with the stronger inhibition of acetone condensation rates by pyridine on $ZrO_2(m)$ than on $TiO_2(a)$.[31]

Seven distinct O atoms (O_a−O_g sites, Scheme 3; CN 2−4, Table 2) are exposed at $ZrO_2(m)$ (−111) surfaces. Their DFT-derived BF_3 affinities (E_{BA}, eq 2) become more negative (0 to −162 kJ mol^{-1}) with decreasing O atom coordination (CN 4 to 2), as expected from the stronger basicity of coordinatively unsaturated O anions. The E_{BA} values exponentially averaged[52] over these distinct O sites on $ZrO_2(m)$ (−111) (−153 kJ mol^{-1}, Table 2) are more negative than those for the two distinct O atoms exposed at $TiO_2(a)$ (101) (−84 kJ mol^{-1}, Table 2), in agreement with the stronger inhibition of acetone condensation rates by CO_2 on $ZrO_2(m)$ than on $TiO_2(a)$.[31]

These distinct Zr and O sites on $ZrO_2(m)$ (−111) (Scheme 3) influence the extent of dissociation of acid-derived species, which depends on the sum of the NH_3 and BF_3 affinities for the Zr and O atoms in each pair ($E_{AA\text{-}Zr} + E_{BA\text{-}O}$). The O−H bond in AcOH* lengthens from 0.107 to 0.150 nm as the ($E_{AA\text{-}Zr}$ + $E_{BA\text{-}O}$) values for Zr−O pairs become more negative (−136 to −264 kJ mol^{-1}; Figure 4a), indicative of more favorable dissociation. For instance, Zr_B−O_c and Zr_A−O_c pairs ($E_{AA\text{-}Zr}$ + $E_{BA\text{-}O}$ −257 and −264 kJ mol^{-1}, respectively, Table 2) dissociate AcOH* to AcO* and a H atom (Scheme 4a,b), in spite of their very different Zr−O distances (0.218 vs 0.375

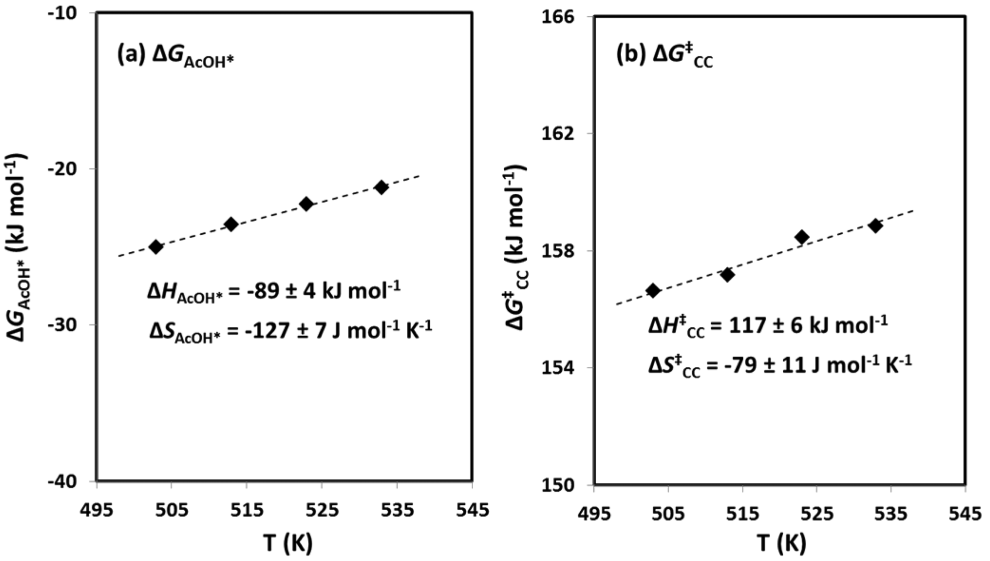

Figure 3. Measured (a) ΔG_{AcOH*} and (b) $\Delta G^{\ddagger}_{CC}$ for ethanoic acid ketonization on ZrO_2(m) as a function of reaction temperature. Dashed lines represent linear regression fits ($\Delta G = \Delta H - T\Delta S$); regressed enthalpy and entropy values are shown beside the respective lines.

Table 2. Coordination Numbers (CN), NH_3 Affinities (E_{AA}), and BF_3 Affinities (E_{BA}) for Exposed Atoms on ZrO_2(m) (−111) and TiO_2(a) (101) Surfaces Shown in Scheme 3

surface	site	CN	E_{AA}[a] (kJ mol^{-1})	E_{BA}[a] (kJ mol^{-1})
ZrO_2(m) (−111)	Zr_A	6	−102	
	Zr_B	6	−95	
	Zr_C	6	−100	
	O_a	4		<−1
	O_b	3		−82
	O_c	2		−162
	O_d	3		−44
	O_e	3		−36
	O_f	3		−97
	O_g	4		<−1
TiO_2(a) (101)	Ti	5	−111	
	O_h	2		−87
	O_i	3		−31

[a] PBE + D3BJ functionals, PAW.

nm). The H−O bond in AcOH increases from 0.099 nm in gaseous species to 0.148−0.150 nm as the acid O atom interacts with a Zr_B or Zr_A center (Zr−O distance: 0.123 nm) and the H atom in the acid OH group interacts with a surface O_c site (H−O distance: 0.105 nm) (Scheme 4a,b); such distances are consistent with the full dissociation of the O−H bond in the acid and with H-bonding between the AcO* and OH* that formed. In contrast, AcOH adsorbs on Zr_B−O_d pairs of weaker combined NH_3 and BF_3 affinity ($E_{AA\text{-}Zr} + E_{BA\text{-}O}$ = −139 kJ mol^{-1}, Table 2) in molecular form (AcOH*, Scheme 4c) with the H−O bond in AcOH* only slightly longer than that in AcOH(g) (0.109 vs 0.099 nm, Scheme 4c).

The adsorption free energies of AcOH-derived bound species (ΔG_{ads}, referenced to a bare ZrO_2(m) (−111) surface and a gaseous acid molecule henceforth) also become more negative from −26 to −101 kJ mol^{-1} (523 K, 1 bar AcOH henceforth) as the combined NH_3 and BF_3 affinity of the Zr−O pair increases ($E_{AA\text{-}Zr} + E_{BA\text{-}O}$, from −136 to −264 kJ mol^{-1}, Figure 4b). This trend is consistent with the concerted interactions of such species with the Zr and O atoms in the site pair.

AcOH can also dissociate at Zr−O−Zr sites (e.g., Zr_A−O_c−Zr_B sites) to form a bidentate carboxylate (*AcO*), in which each of its two O atoms is bound to a Zr center and the dissociated hydroxyl H atom interacts with one of the surface O atoms (Scheme 4d). The O atoms in *AcO* species bound at Zr_A−O_c−Zr_B sites are closer to Zr_A than to Zr_B (0.225 vs 0.230 nm, Scheme 4d), in agreement with its more negative NH_3 affinity (E_{AA} −102 vs −95 kJ mol^{-1}, Table 2).

The ΔG_{ads} values for *AcO* among all types of Zr−O−Zr sites on ZrO_2(m) (−111) surfaces range from −85 to −140 kJ mol^{-1} (Table 3; geometry parameters for each DFT-derived *AcO* shown in Table S1, SI). The most stable *AcO* species bind each of their two O atoms to the Zr_A and Zr_B sites and the H atom to the O_c site (ΔG_{ads} −140 kJ mol^{-1}, Table 3), while the least stable *AcO* is connected to the same Zr_A and Zr_B centers but with the H atom at the O_d site (ΔG_{ads} −85 kJ mol^{-1}, Table 3). This reflects the greater basicity of O_c than O_b sites (E_{BA} −162 vs −82 kJ mol^{-1}, Table 2).

AcOH*, AcO*, and *AcO* species bound on ZrO_2(m) surfaces differ in their respective carboxyl (C(═O)OH) or carboxylate (C(═O)O) stretch modes, all of which appear in the 1350−1800 cm^{-1} wavenumber range (Table 4). Specifically, DFT-derived frequencies for C═O and C—O vibrations ($\nu_{C=O}$ and ν_{C-O}) in AcOH* are 1610−1646 and 1491−1517 cm^{-1}, respectively. The frequencies for the respective antisymmetric and symmetric carboxylate vibrations ($\nu_{COO,as}$ and $\nu_{COO,s}$) in AcO* are 1512−1584 and 1392−1408 cm^{-1}. Such $\nu_{COO,as}$ and $\nu_{COO,s}$ values for bidentate *AcO* bound at diverse Zr—O—Zr sites on ZrO_2(m) are 1529−1559 and 1435−1450 cm^{-1}, respectively. These different bands for carboxyl (C(═O)OH) and carboxylate (C(═O)O) stretch modes are used next to experimentally confirm the various types of acid-derived species bound to ZrO_2(m) during catalytic ketonization catalysis.

3.4. Infrared Assessment of the Relative Coverages of Acid-Derived Species During Ketonization Catalysis.

Figure 5 compares infrared spectra of ZrO_2(m) before and after contact with AcOH (0.2−1.6 kPa) at 523 K. ZrO_2(m) samples treated in He at 573 K for 2 h show weak and broad bands centered at 1543 and 1448 cm^{-1} before contact with

Scheme 3. Structures of ZrO_2(m) (−111) and TiO_2(a) (101) Surfaces and Respective Metal and Oxygen Centers Exposed on Each Unit Cell of These Surfaces

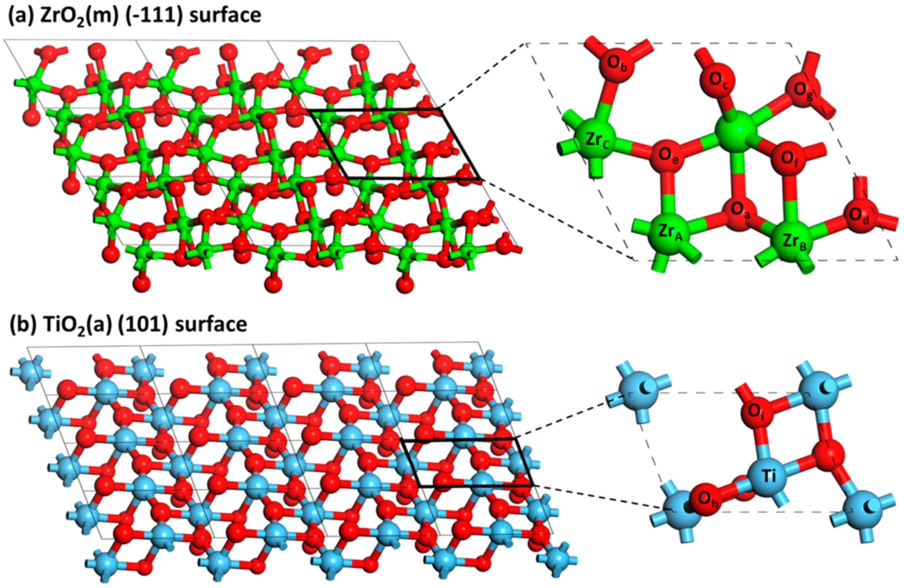

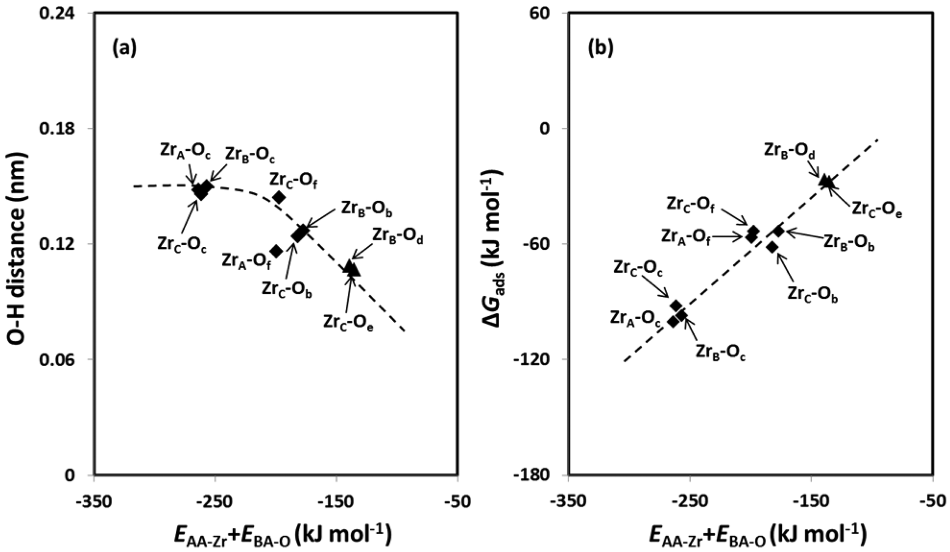

Figure 4. (a) DFT-derived O−H distance in AcOH-derived species bound at a Zr−O pair of ZrO_2(m) (−111) surfaces and (b) the respective adsorption free energies (ΔG_{ads}) as a function of the combined NH_3 and BF_3 affinity of the Zr−O pair ($E_{AA\text{-}Zr} + E_{BA\text{-}O}$) (AcO* (♦), AcOH* (▲); PBE+D3BJ, PAW, 523 K, 1 bar AcOH; denotation of the Zr and O sites shown in Scheme 3). Dashed lines represent qualitative trends.

AcOH(g). These bands arise from carbonates formed upon contact with CO_2 present in ambient air.[53] We surmise that these carbonates do not interfere with ketonization catalysis on ZrO_2(m), because of their high stability and low coverages at ketonization reaction conditions. Several infrared bands appeared in the 1300−1800 cm^{-1} range (1797, 1778, 1684, 1590, 1521, 1460, and 1393 cm^{-1}) upon contact of ZrO_2(m) with 0.2 kPa AcOH at 523 K (Figure 5). The bands at 1797 and 1778 cm^{-1} correspond to carboxyl vibrations in AcOH(g),[54] and their intensities increase linearly with AcOH pressure (0.2−1.6 kPa, Figure S2, SI). The DFT-derived frequencies in Table 4 indicate that the other bands correspond to vibrations in AcOH* ($\nu_{C=O}$ 1684 cm^{-1}), AcO* ($\nu_{COO,as}$ 1590 cm^{-1}; $\nu_{COO,s}$ 1393 cm^{-1}), and *AcO* ($\nu_{COO,as}$ 1521 cm^{-1}; $\nu_{COO,s}$ 1460 cm^{-1}). The carboxylate vibrations for AcO* and *AcO* show similar intensities that are ~500-fold greater than for C=O vibrations in AcOH* of similar infrared absorption cross sections (Figure 5). These data indicate that dissociated forms of ethanoic acid prevail over their molecular analogues on ZrO_2(m). The intensity of the carboxylate bands (AcO* and *AcO*) is almost insensitive to the acid pressure within 0.2−1.6 kPa (Figure 5), indicative of nearly saturated coverages by AcO* and *AcO* at AcOH pressures relevant to ketonization catalysis, as also shown by the kinetic analysis in Section 3.2. The overlap between these infrared bands for AcO* and *AcO* and the weaker band for AcOH*, however, prevents an accurate determination of AcOH* coverages on ZrO_2(m).

The removal of AcOH(g) from the He stream led to the immediate disappearance of the bands for AcOH(g) and AcOH* at 523 K, while those for AcO* and *AcO* decreased only slightly during a 2 h period (Figure 5). The slow removal of AcO* and *AcO* from ZrO_2(m) surfaces reflects their

Scheme 4. DFT-Derived Adsorption Modes of Ethanoic Acid on Zr−O Site Pairs of ZrO_2(m) (−111) Surfaces (PBE+D3BJ, PAW)

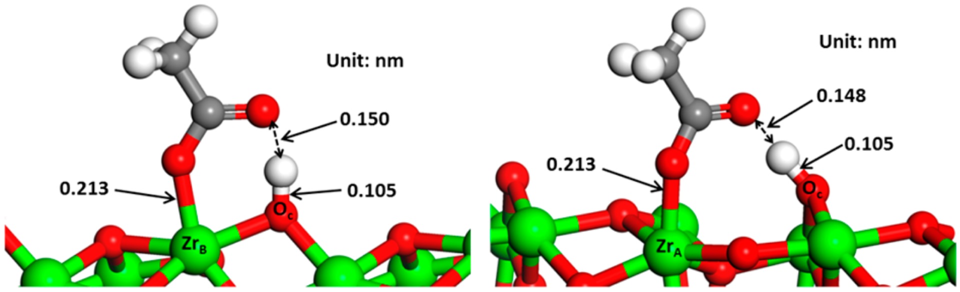
(a) AcO* on a bonded Zr-O pair

(b) AcO* on a unbonded Zr-O pair

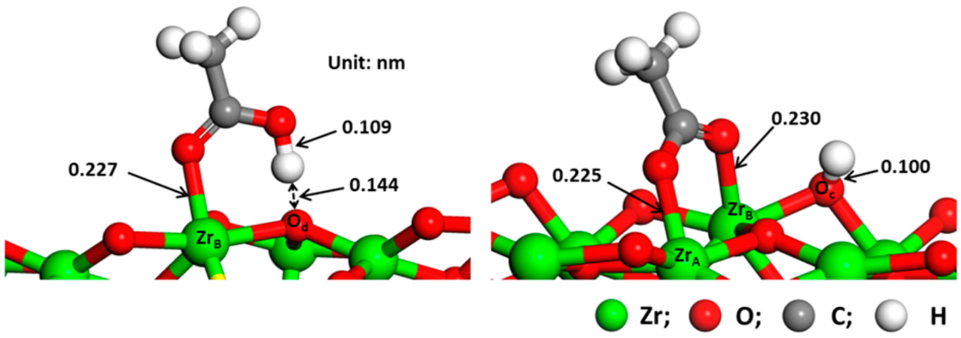
(c) AcOH* on a Zr-O pair

(d) *AcO* on two Zr-O pairs

Table 3. DFT-Derived Adsorption Free Energy (ΔG_{ads}) and Respective Enthalpy and Entropy Components for Ethanoic Acid Adsorption on Zr−O−Zr Sites of ZrO_2(m) (−111) Surfaces[a]

Zr−O−Zr sites[b]	ΔG_{ads} (kJ mol^{-1})	ΔH_{ads} (kJ mol^{-1})	ΔS_{ads} (J mol^{-1} K^{-1})
Zr_A−O_c−Zr_B	−140	−236	−184
Zr_A−O_c−Zr_C	−129	−228	−188
Zr_A−O_b−Zr_B	−85	−186	−194

[a] PBE+D3BJ, PAW, *AcO*, 523 K, 1 bar ethanoic acid. [b] Denotation of Zr and O sites shown in Scheme 3.

Table 4. DFT-Derived Vibrational Frequencies for Adsorption Modes of Ethanoic Acid on Zr−O Site Pairs of ZrO_2(m) (−111) Surfaces[a]

binding sites[b]	mode	vibrational frequency (cm^{-1})			
		$\nu_{C=O}$	ν_{C-O}	$\nu_{COO,as}$	$\nu_{COO,s}$
Zr_B—O_d	AcOH*	1646	1491		
Zr_C—O_e	AcOH*	1610	1517		
Zr_A—O_c	AcO*			1584	1408
Zr_B—O_c	AcO*			1583	1392
Zr_C—O_c	AcO*			1573	1408
Zr_B—O_b	AcO*			1512	1398
Zr_C—O_b	AcO*			1523	1395
Zr_A—O_f	AcO*			1543	1400
Zr_A—O_c—Zr_B	*AcO*			1559	1444
Zr_A—O_c—Zr_C	*AcO*			1540	1435
Zr_A—O_b—Zr_B	*AcO*			1529	1450

[a] PBE+D3BJ, PAW, 523 K, 1 bar ethanoic acid. [b] Denotation of Zr and O sites shown in Scheme 3.

strong binding at Zr−O pairs, in contrast with the weak binding of AcOH* species, which equilibrate rapidly with AcOH(g).

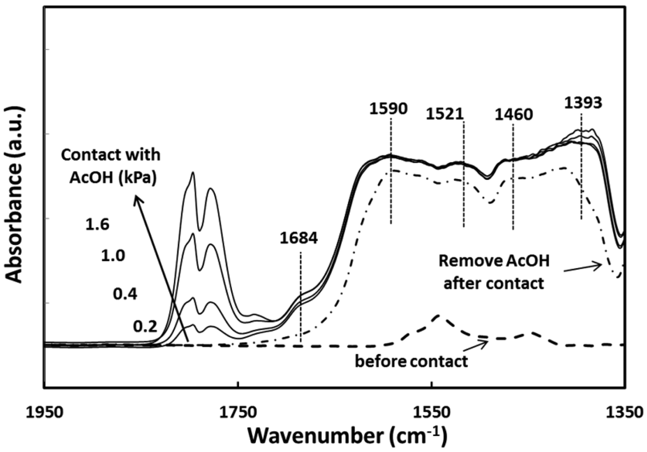

Figure 5. IR spectra of ZrO_2(m) with 0.2−1.6 kPa ethanoic acid during ketonization at 523 K (spectra before (---) and after (-·-) the acid contact shown as reference).

The kinetic analysis in Section 3.2 cannot discern the relative contributions of AcO* and *AcO* species to C−C bond formation without the benchmarking with theory described in the next section.

3.5. Theoretical Assessment of Ketonization Elementary Steps and Reactivity of Adsorbed Species on Monoclinic ZrO_2 Surfaces.

The elementary steps shown in Scheme 1 for ketonization reactions are examined next using DFT methods and AcOH as the illustrative reactant on the ZrO_2(m) (−111) surfaces that prevail on ZrO_2(m) powders.[24] These methods include Grimme's D3BJ dispersion corrections[43] to account for van der Waals interactions among coadsorbed acid reactants, which become significant at the near saturation coverages evident from kinetic and infrared data shown above (Table 1 and Figure 5). All calculations are

Scheme 5. DFT-Derived Structures for Adsorbed Acid Reactants and Transition States Involved in Ketonization of AcO* and AcOH* on Zr−O Pairs of ZrO_2(m) (−111) Surfaces (PBE+D3BJ, PAW, $^2/_3$ML Acid Coverage)[a]

(a) Coadsorption of AcO* and AcOH* (b) TS for enolization of AcO*

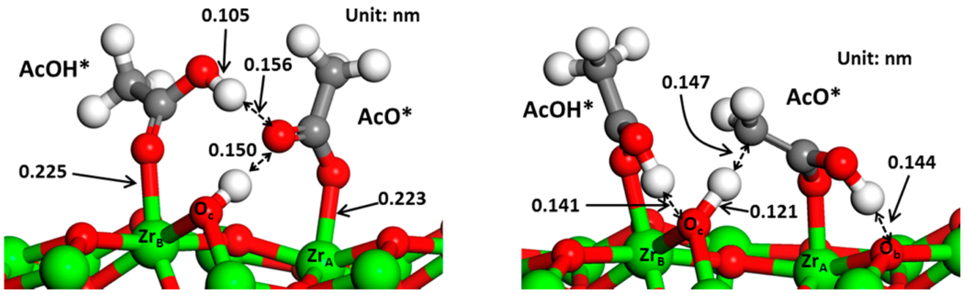

(c) TS for C-C coupling with AcOH* (d) TS for intramolecular dehydration

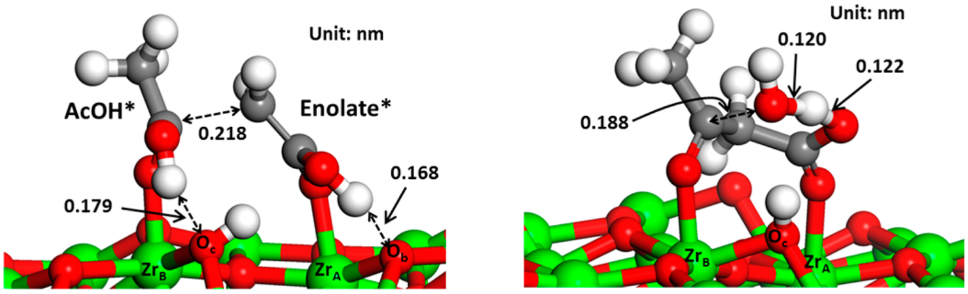

(e) TS for decarboxylation to enolate (f) TS for protonation of enolate

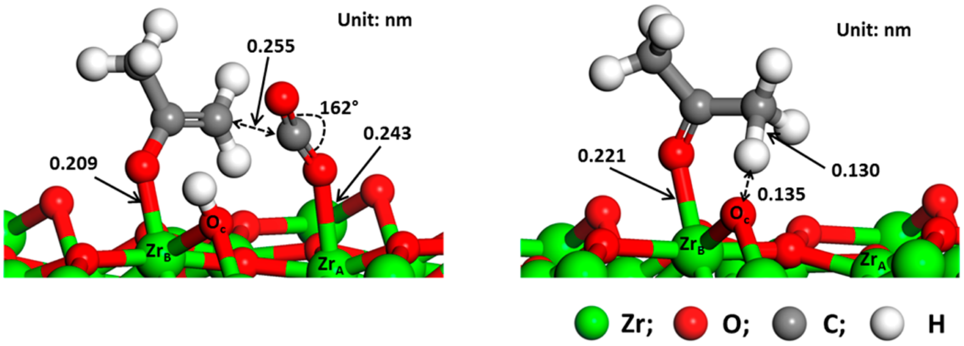

[a] Irrelevant coadsorbed acids are not shown for clarity.

carried out using a unit cell of ZrO_2(m) (−111) and two AcOH-derived species, corresponding to a fractional surface coverage (θ_{acid}) of $^2/_3$ML. Here θ_{acid} is defined as the ratio of adsorbed carboxylic acid molecules (n_{acid}) to exposed Zr−O pairs (n_{Zr-O}):

$$\theta_{acid} = \frac{n_{acid}}{n_{Zr-O}}(ML) \tag{8}$$

By these definitions, the maximum attainable θ_{acid} values are 1 ML for monodentate configurations (AcO* and AcOH*) and $^1/_2$ML for bidentate configurations (*AcO*).

Ketonization steps involving coadsorbed AcO* and AcOH* bound at Zr_A−O_c−Zr_B sites are examined first. DFT-optimized structures for AcOH* bound to a Zr_B center next to a coadsorbed AcO* species at a Zr_A−O_c pair show that the OH group in AcOH* H-bonds to one of the carboxylate O atoms in AcO* (H−O distance 0.156 nm; Scheme 5a), instead of interacting via H-bonding to a lattice O atom at low acid coverages ($^1/_3$ML AcOH*, Scheme 4c). Such AcOH* configurations prevail at acid coverages above $^2/_3$ML, because strongly basic O sites are blocked by adsorbed species at such coverages.

The cleavage of the α-C−H bond in AcO* leads to the formation of 1-hydroxy enolates (step 3, Scheme 1). These species then carry out a nucleophilic attack at coadsorbed AcOH* species to form the new C−C bond (step 4, Scheme 1). Scheme 5b shows the DFT-derived transition state (TS) for α−C−H cleavage in AcO* at the Zr_A−O_c pair in the presence of coadsorbed AcOH*. The bonds incipiently cleaved (α-C−H, 0.147 nm, Scheme 5b) and formed (H−O_c, 0.121 nm) at the enolization TS are longer than the α-C−H bond in the reactant state (0.110 nm) and the fully formed H−O_c bond in the product state (0.102 nm, Scheme S1, SI), respectively, consistent with the concerted nature of a TS that occurs at an intermediate point along the reaction coordinate.

The terminal C atom in the 1-hydroxy enolate then attacks the carboxyl C atom in AcOH* to form a new C−C bond (step 4, Scheme 1) through a TS with a C−C distance of 0.218 nm (Scheme 5c) shorter than the combined van der Waals radii of the two C atoms (0.340 nm), but longer than the C−C bond in the product state (0.156 nm, Scheme S1, SI). As in the case of

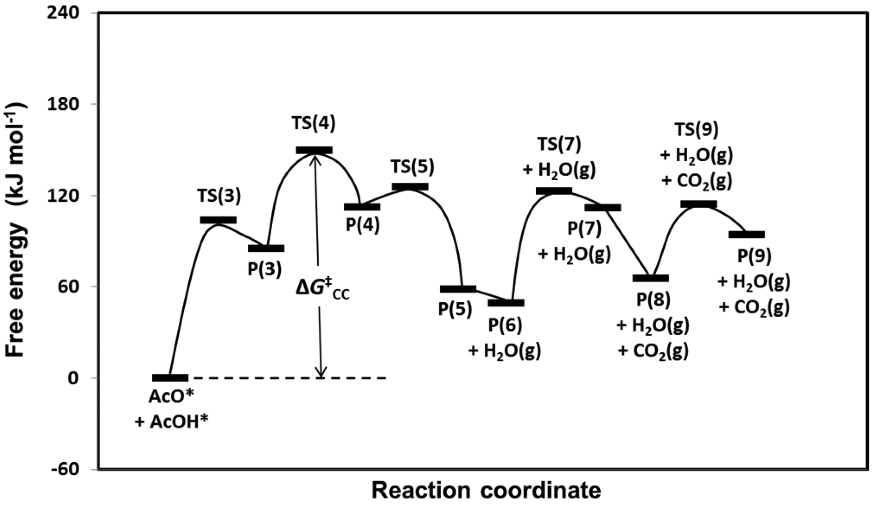

Figure 6. DFT-derived free energy reaction coordinate diagram for ketonization of AcO* and AcOH* on ZrO_2(m) (−111) surfaces (PBE+D3BJ, PAW; 523 K, 1 bar ethanoic acid, $^2/_3$ML acid coverage). All energy values are referenced to an AcO*−AcOH* reactant pair. Only key surface intermediates and transition states are shown for clarity. TS(x) and P(x) represent respective transition state and product of step x in Scheme 1.

Table 5. DFT-Derived ΔG_{AcOH*}, $\Delta G^{\ddagger}_{CC}$ and Corresponding Enthalpy and Entropy Components and Isotope Effects for Ethanoic Acid Ketonization on ZrO_2(m) (−111) Surfaces[a]

enolate donor[b]	acid donor[c]	ΔH_{AcOH*} (kJ mol^{-1})	ΔS_{AcOH*} (J mol^{-1} K^{-1})	ΔG_{AcOH*} (kJ mol^{-1})	$\Delta H^{\ddagger}_{CC}$ (kJ mol^{-1})	$\Delta S^{\ddagger}_{CC}$ (J mol^{-1} K^{-1})	$\Delta G^{\ddagger}_{CC}$ (kJ mol^{-1})	$\frac{(K_2)_H}{(K_2)_D}$	$\frac{(\overrightarrow{k_4K3})_H}{(\overrightarrow{k_4K3})_D}$
AcO*	AcOH*	−113	−185	−17	127	−42	149	1.0	1.2
AcO	AcOH*	−123	−196	−20	203	−56	232	1.0	1.2

[a] PBE+D3BJ, PAW, 523 K, 1 bar ethanoic acid, $^2/_3$ML acid coverage. [b] The acid reactant that forms 1-hydroxy enolate in the C−C coupling step (step 4, Scheme 1). [c] The acid reactant that is attacked by the 1-hydroxy enolate in the C−C coupling step (step 4, Scheme 1).

enolate formation, the C−C bond formation TS also involves concerted interactions with the Zr and O centers and occurs at an intermediate point along the reaction coordinate. The OH groups in AcOH* and 1-hydroxy enolate species are H-bonded to vicinal O_c and O_b sites, respectively (H−O distance: 0.179 and 0.168 nm, Scheme 5c), as also observed on TiO_2(a) surfaces.[23]

A H_2O molecule is eliminated from the α-hydroxy γ-carboxy alkoxides formed (step 5, Scheme 1) by intramolecular H-transfer from its COOH to its OH group, as also observed on TiO_2(a) (101) and TiO_2(r) (110).[23] The H atom lies nearly equidistant between the donor and acceptor O atoms at the elimination TS (O—H distance: 0.122 and 0.120 nm, respectively, Scheme 5d), in which the C—O bond between the O atom at the OH group and the α-C atom in the alkoxide lengthens from 0.153 nm (in the reactant state, Scheme S1, SI) to 0.188 nm at the TS. These C—O and O—H distances indicate that the cleavage of C—O bond and the formation of H—O bond for the elimination of H_2O from the α-hydroxy γ-carboxy alkoxides occur in a concerted manner. The β-keto carboxylates formed in the H_2O elimination step then decarboxylate to form propen-2-olate and CO_2 (step 7, Scheme 1) via a TS in which the C—C bond between the enolate and carboxylate moieties in β-keto carboxylates lengthens from 0.154 nm (in the reactant state, Scheme S1, SI) to 0.255 nm (Scheme 5e) at the TS state, concurrently with O—C—O angles in the carboxylate group that increase from 125° at the reactant state to 162° at the TS (vs 180° in CO_2(g)). The propen-2-olates formed in the decarboxylation steps are protonated to acetone by the H atom stranded at the O_c site in the step that cleaves the α-C—H bond in AcO* (step 9, Scheme 3). The TS that mediates this reprotonation step involves the incipient cleavage of H—O_c bonds (0.135 nm) and formation of α-C—H bonds (0.130 nm) of similar length (Scheme 5f), indicative of O_c sites and terminal C atoms (at the C=C bond in propen-2-olate) of similar proton affinity.

DFT-derived free energies for all intermediate and TS structures involved in the ketonization elementary steps are reported in Figure 6 (523 K, 1 bar AcOH, $^2/_3$ML AcOH henceforth; enthalpies shown Figure S3, SI). These free energies (referenced to a AcO*−AcOH* reactant pair) are all positive (Figure 6), indicative of their reduced stability and lower coverages than the AcO*−AcOH* reactant pairs on ZrO_2(m) surfaces at ketonization reaction conditions. The C−C coupling TS (TS(4), Figure 6) exhibits a free energy of 149 kJ mol^{-1}, which is higher than for any intermediates or other TS structures along the reaction coordinate. Consequently, this C−C coupling step is irreversible, and the sole kinetically relevant elementary step in ketonization reactions of AcO*−AcOH* coadsorbed species on ZrO_2(m) (−111) surfaces.

The formation free energies of the C−C coupling TS from AcO*−AcOH* reactant pairs ($\Delta G^{\ddagger}_{CC}$, Scheme 2) determine the kinetic constant $\overrightarrow{k_4}K_3$ in the numerator of the rate equation (eq 3). DFT-derived $\Delta G^{\ddagger}_{CC}$ values for ethanoic acid reactants on ZrO_2(m) (149 kJ mol^{-1}, Table 5) are similar to those calculated from measured rates (158 ± 1 kJ mol^{-1}, Table 1), as is the case also for their enthalpy components (127 vs 117 ± 6 kJ mol^{-1}, Figure 3 and Table 5). DFT-derived and measured values for $(\overrightarrow{k_4}K_3)_H/(\overrightarrow{k_4}K_3)_D$ are also in agreement (1.2 vs 1.2 ± 0.1, Tables 1 and 5), thus confirming the sole kinetic relevance

Scheme 6. Proposed Elementary Steps for Ketonization of *AcO* and AcOH* on ZrO_2(m) Surfaces with Asymmetric Acid−Base Zr−O Site Pairs[a]

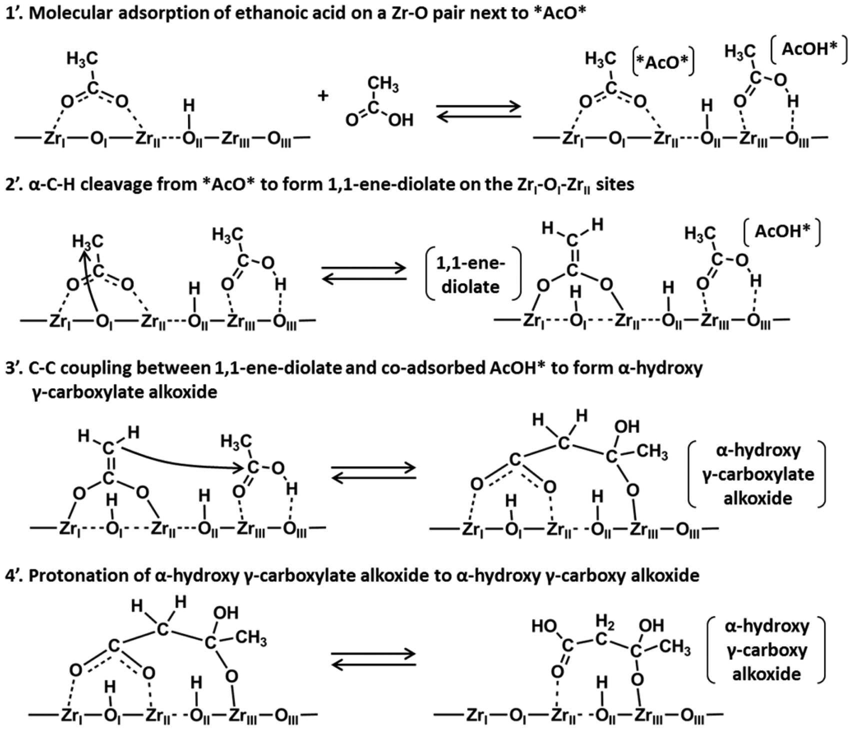

[a] Zr_I−O_I−Zr_{II}−O_{II}−Zr_{III}−O_{III} sites represent a catalytically relevant domain exposed on ZrO_2(m).

Scheme 7. DFT-Derived Structures for Adsorbed Acid Reactants and Transition States Involved in Ketonization of *AcO* and AcOH* on Zr−O Pairs of ZrO_2(m) (−111) Surfaces (PBE+D3BJ, PAW, $^2/_3$ML Acid Coverage)[a]

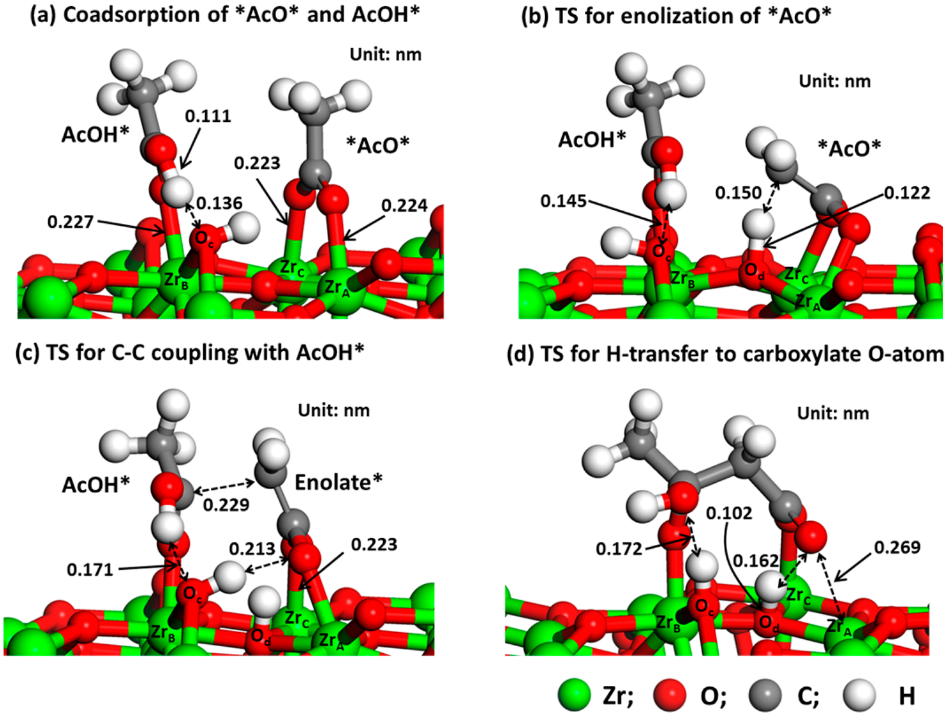

[a] Irrelevant coadsorbed acids are not shown for clarity.

of the C−C coupling step (step 4, Scheme 1) in the ketonization of ethanoic acid on ZrO_2(m).

The formation free energy of AcOH* species vicinal to AcO* species from AcOH(g) (ΔG_{AcOH*}, Scheme 2) determines the value of K_2 in eq 3. These DFT-derived ΔG_{AcOH*} values on ZrO_2(m) (−17 kJ mol^{-1}, Table 5), as well as the $(K_2)_H/(K_2)_D$ values (1.0, Table 5), agree well with measured values (−22 ± 1 kJ mol^{-1} and 1.0 ± 0.1, Table 2). The enthalpy and entropy

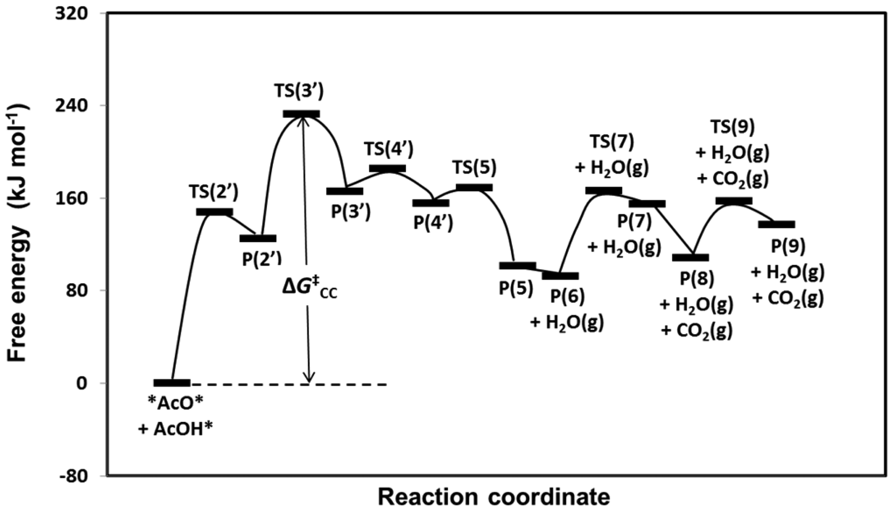

Figure 7. DFT-derived free energy reaction coordinate diagram for ketonization of *AcO* and AcOH* on ZrO_2(m) (−111) surfaces (PBE+D3BJ, PAW; 523 K, 1 bar ethanoic acid, $^2/_3$ML acid coverage). All energy values are referenced to an *AcO*−AcOH* pair. Only key surface intermediates and transition states are shown for clarity. TS(x) and P(x) represent the respective transition state and product of step x in Scheme 1, whereas TS(x') and P(x') represent the respective transition state and product of step x' in Scheme 6.

components of ΔG_{AcOH*} from DFT are, however, both more negative than the measured values (ΔH_{AcOH*} −113 vs −89 ± 4 kJ mol^{-1}, ΔS_{AcOH*} −185 vs −127 ± 7 kJ mol^{-1}, Figure 3 and Table 5); these discrepancies reflect the stronger binding and less mobile nature of species optimized using Grimme's D3BJ dispersion corrections with PBE functionals.[23,42,43]

Ketonization steps involving coadsorbed *AcO* and AcOH* reactants bound at Zr_A−O_c−Zr_c and Zr_B−O_c sites are examined next, in order to contrast with AcO*−AcOH* reactions described above and to examine the proposed intermediate role of bidentate carboxylates in ketonization catalysis.[11−26] As for AcO*−AcOH* reactant pairs (Scheme 1), α-H abstraction in *AcO* by an O site leads to 1,1-ene-diolates (step 2′, Scheme 6), which then nucleophilically attack the carboxylic C atom in AcOH* to form α-hydroxy γ-carboxylate alkoxides (step 3′, Scheme 6). The protonation of the γ-carboxylate group in such alkoxides leads to α-hydroxy γ-carboxy alkoxides (step 4′, Scheme 6), which undergo subsequent dehydration, decarboxylation, and protonation steps identical to those that mediate AcO*−AcOH* reactions (steps 5−10, Scheme 1).

Scheme 7a shows DFT-derived structures for *AcO* bound at Zr_A and Zr_C centers via its two O atoms with its dissociated H atom at the O_c site and a coadsorbed AcOH* at a Zr_A site with its OH group H-bonded to the same O_c as *AcO* (H−O_c distance 0.136 nm). 1,1-Ene-diolates are formed by abstraction of the α-H in *AcO* by an O_d site (step 2′, Scheme 6); the distances between the α-H atom and the O_d site at the α-C−H cleavage TS are longer than those in the product state (0.122 vs 0.102 nm, Scheme 7b), and the α-H−C distance at the TS is longer than in the *AcO* reactant state (0.150 vs 0.110 nm, Scheme 7b), again indicative of the concerted nature of this TS structure, as also found for the enolization of AcO* at a Zr_A−O_c site pair (Scheme 5b).

The C−C coupling reactions between 1,1-ene-diolates and coadsorbed AcOH* species are mediated by a TS similar to that for reactions of 1-hydroxy enolates (derived from AcO*) with AcOH* (0.229 vs 0.218 nm C−C bond at the TS; Schemes 5c and 7c), but the 1,1-ene-diolate moiety at the TS is bound to Zr_A and Zr_C centers instead of the single Zr_A center that interacts with the 1-hydroxy enolate. The α-hydroxy γ-carboxylate alkoxides formed from bound 1,1-ene-diolates and AcOH* convert to the same α-hydroxy γ-carboxy alkoxide derived from AcO*−AcOH* reactants; this reaction involves the transfer of a proton bound at O_d sites to the Zr_A-bound O atom in the α-hydroxy γ-carboxylate alkoxide (Scheme 7d).

As for the routes mediated by AcO*−AcOH* pairs, the C−C coupling TS (TS(3′), Figure 7) for reactions of *AcO*−AcOH* pairs exhibits the highest free energy among all species along the reaction coordinate (232 kJ mol^{-1}; referenced to an *AcO*−AcOH* pair; enthalpies in Figure S4, SI). These free energies also show that *AcO*−AcOH* pairs are more stable than other intermediates; the *AcO*−AcOH* free energies are the lowest among all intermediates (Figure 7). Thus, C−C coupling is the sole kinetically relevant step, and *AcO*−AcOH* pairs are the most abundant surface species (MASI). Consequently, ketonization rates via *AcO*−AcOH* pairs reflect the formation free energy of the C−C coupling TS from *AcO*−AcOH* pairs ($\Delta G^{\ddagger}_{CC}$, Figure 7). DFT-derived ΔG_{AcOH*} values for *AcO*−AcOH* (−20 kJ mol^{-1}; Table 4) and AcO*−AcOH* (−17 kJ mol^{-1}) pairs are similar, but $\Delta G^{\ddagger}_{CC}$ values for *AcO*−AcOH* routes are much larger than for those involving AcO*−AcOH* pairs (232 vs 149 kJ mol^{-1}, Table 4). The $(\overrightarrow{k_4}K_3)_{AcO*\text{-}AcOH*}/(\overrightarrow{k_4}K_3)_{*AcO*-AcOH*}$ ratio derived from these $\Delta G^{\ddagger}_{CC}$ values is 1.9×10^8 (523 K), implying that bidentate carboxylates would not contribute to measured ketonization rates.

These DFT-derived free energies show that reactions of AcO* with AcOH* are much more facile than those of *AcO* and that monodentate AcO* and AcOH* are the reactive ketonization intermediates and bidentate *AcO* species are unreactive, because of their strong binding onto Zr−O site pairs. These conclusions are similar to those reached from kinetic, spectroscopic, and theoretical studies on TiO_2[23] and seem also applicable to the ketonization of C_3 and C_4 carboxylic acids, which exhibit similar kinetic behavior as ethanoic acid on both ZrO_2 (Section 3.1) and TiO_2[23] catalysts.

3.6. Consequences of Acid−Base Strength for Ketonization Reactivity on Metal Oxides.

Ketonization of carboxylic acids occurs on ZrO_2(m) and TiO_2(a) surfaces nearly saturated by acid-derived bound species via C−C coupling between acid-derived 1-hydroxy as enolates and coadsorbed acids. Therefore, the $\Delta G^{\ddagger}_{\mathrm{CC}}$ term (Scheme 2) determines the intrinsic ketonization reactivity on acid–base site pairs of metal oxides. Measured $\Delta G^{\ddagger}_{\mathrm{CC}}$ values for AcOH are 158 ± 1 kJ mol^{-1} on ZrO_2(m) (Table 2) and 166 ± 1 kJ mol^{-1} on TiO_2(a)[23] at 523 K, consistent with DFT-derived free energies (149 vs 160 kJ mol^{-1}, Table 5). These values reflect the different acid–base properties between ZrO_2(m) and TiO_2(a); ZrO_2(m) has stronger basic O sites but weaker Lewis acid centers than TiO_2(a), evident by site titrations with different probe molecules during acetone condensation[31] and by DFT assessments with the exposed site pairs on the most stable ZrO_2(m) and TiO_2(a) surfaces (Section 3.3).

The $\Delta G^{\ddagger}_{\mathrm{CC}}$ term is equal to the sum of the free energy changes upon formation of 1-hydroxy enolates from AcO* on M–O site pairs (M = Ti, Zr; ΔG_e, Scheme 2) and of the C–C coupling TS from its 1-hydroxy-enolate-AcOH* precursors on ZrO_2(m) or 1-hydroxy-enolate-AcO* precursors on TiO_2(a) ($\Delta G^{\ddagger}_{\mathrm{CC,t}}$, Scheme 2). These two free energies determine the steady-state coverages of 1-hydroxy enolates and their intrinsic reactivity for C–C coupling with AcOH* or AcO*, respectively. Ketonization turnover rates reflect their combined contributions, which, however, cannot be separately extracted from such data. DFT treatments show that the ΔG_e component in $\Delta G^{\ddagger}_{\mathrm{CC}}$ is much smaller on ZrO_2(m) than TiO_2(a) (85 vs 111 kJ mol^{-1}, 523 K and 1 bar AcOH, Figure 8), but the $\Delta G^{\ddagger}_{\mathrm{CC,t}}$ component is larger on ZrO_2(m) than TiO_2(a) (64 vs 49 kJ mol^{-1}). Therefore, the more reactive nature of ZrO_2(m) surfaces arises from higher 1-hydroxy enolate coverages on Zr centers (lower ΔG_e), as a result of stronger basic O sites on ZrO_2(m), which disfavor the reprotonation of 1-hydroxy enolates to form AcO*.

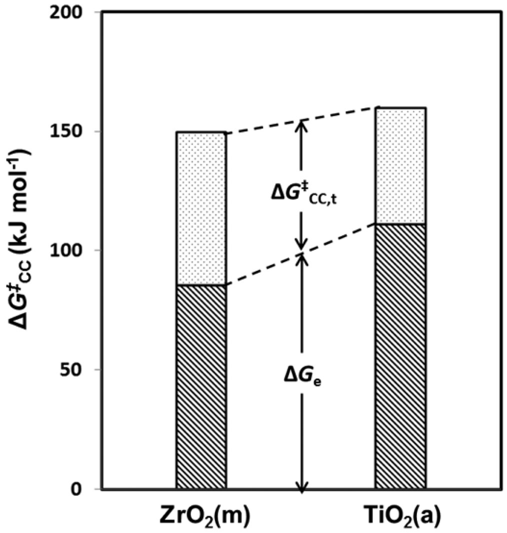

Figure 8. DFT-derived $\Delta G^{\ddagger}_{\mathrm{CC}}$ values and their ΔG_e and $\Delta G^{\ddagger}_{\mathrm{CC,t}}$ components for ketonization of ethanoic acid on ZrO_2(m) (−111) and TiO_2(a) (101) surfaces (PBE+D3BJ, PAW; 523 K, 1 bar ethanoic acid). Data of ZrO_2(m) are adapted from Figure 6, and data of TiO_2(a) are adapted from ref 23

4. CONCLUSIONS

Ketonization reactions of C_2–C_4 carboxylic acids on ZrO_2 and TiO_2 surfaces are both kinetically limited by C–C bond formation between acid-derived 1-hydroxy enolates and coadsorbed acids at acid–base metal–oxygen (M–O) site pairs that are nearly saturated by carboxylates formed from dissociation of adsorbed acids at reaction conditions of catalysis. In contrast to the uniform Ti–O site pairs exposed on TiO_2 surfaces, diverse Zr and O sites of different coordinations and acid/base properties are present on monoclinic ZrO_2 surfaces, resulting in the coexistence of molecularly adsorbed acids and monodentate and bidentate carboxylates on ZrO_2 during catalysis. The binding strength and the dissociation extent of such acid-derived species both increase as the combined acid and base strengths for the Zr and O centers at the site pairs increase, which can be appropriately described by DFT-derived NH_3 and BF_3 affinities, respectively. Monodentate and bidentate carboxylates are the prevalent bound species on monoclinic ZrO_2, while the free energy activation barriers for C–C bond formation from the monodentate carboxylates and coadsorbed acids are much smaller than from the more stable bidentate carboxylates, as a result of energetic penalties to form C–C coupling transition states along their reaction coordinates. Such free energy C–C bond formation activation barriers are lower on monoclinic ZrO_2 than on anatase TiO_2, because the more strongly basic O sites on the former surfaces lead to more stable 1-hydroxy enolates via their stronger bonds with the H atom abstracted from the α-position in the monodentate carboxylate precursors and consequently to smaller activation barriers.

■ ASSOCIATED CONTENT

Ⓢ Supporting Information

The Supporting Information is available free of charge on the ACS Publications website at DOI: 10.1021/acs.jpcc.7b05987.

> Space velocity effects for ketonization rates on ZrO_2, intensity of infrared bands for gaseous ethanoic acid as a function of the acid pressure, DFT-derived structures for bound acids and ketonization reaction intermediates, and enthalpy reaction coordinate diagrams for ketonization on ZrO_2 (PDF)

■ AUTHOR INFORMATION

Corresponding Author

*Fax: + 1 510-642-4778. E-mail: iglesia@berkeley.edu. Phone: + 1 925-323-5559.

ORCID

Enrique Iglesia: 0000-0003-4109-1001

Notes

The authors declare no competing financial interest.

■ ACKNOWLEDGMENTS

We acknowledge with thanks the financial support of this research from BP p.l.c. via the XC^2 program at UC-Berkeley. We are also grateful for the valuable technical advice from Drs. Eric Doskocil, John Shabaker, Glenn Sunley, and all other members involved in the BP XC^2 program during this study. The Extreme Science and Engineering Discovery Environment (XSEDE) provided the access to computational facilities, which is supported by National Science Foundation (Grant ACI-1548562).

■ REFERENCES

(1) Renz, M. Ketonization of Carboxylic Acids by Decarboxylation: Mechanism and Scope. *Eur. J. Org. Chem.* **2005**, *2005*, 979–988.

(2) Pham, T. N.; Sooknoi, T.; Crossley, S. P.; Resasco, D. E. Ketonization of Carboxylic Acids: Mechanisms, Catalysts, and Implications for Biomass Conversion. *ACS Catal.* **2013**, *3*, 2456−2473.

(3) Pacchioni, G. Ketonization of Carboxylic Acids in Biomass Conversion over TiO_2 and ZrO_2 Surfaces: A DFT Perspective. *ACS Catal.* **2014**, *4*, 2874−2888.

(4) Foraita, S.; Fulton, J. L.; Chase, Z. A.; Vjunov, A.; Xu, P.; Barath, E.; Camaioni, D. M.; Zhao, C.; Lercher, J. A. Impact of the Oxygen Defects and the Hydrogen Concentration on the Surface of Tetragonal and Monoclinic ZrO_2 on the Reduction Rates of Stearic Acid on Ni/ZrO_2. *Chem. - Eur. J.* **2015**, *21*, 2423−2434.

(5) Gaertner, C. A.; Serrano-Ruiz, J. C.; Braden, D. J.; Dumesic, J. A. Catalytic Coupling of Carboxylic Acids by Ketonization as a Processing Step in Biomass Conversion. *J. Catal.* **2009**, *266*, 71−78.

(6) Crisci, A. J.; Dou, H.; Prasomsri, T.; Román-Leshkov, Y. Cascade Reactions for the Continuous and Selective Production of Isobutene from Bioderived Acetic Acid over Zinc-Zirconia Catalysts. *ACS Catal.* **2014**, *4*, 4196−4200.

(7) Bond, J. Q.; Upadhye, A. A.; Olcay, H.; Tompsett, G. A.; Jae, J.; Xing, R.; Alonso, D. M.; Wang, D.; Zhang, T.; Kumar, R.; et al. Production of Renewable Jet Fuel Range Alkanes and Commodity Chemicals from Integrated Catalytic Processing of Biomass. *Energy Environ. Sci.* **2014**, *7*, 1500−1523.

(8) Mekhemer, G. A. H.; Halawy, S. A.; Mohamed, M. A.; Zaki, M. I. Ketonization of Acetic Acid Vapour over Polycrystalline Magnesia: In situ Fourier Transform Infrared Spectroscopy and Kinetic Studies. *J. Catal.* **2005**, *230*, 109−122.

(9) Gliński, M.; Kijeński, J.; Jakubowski, A. Ketones from Monocarboxylic Acids: Catalytic Ketonization over Oxide Systems. *Appl. Catal., A* **1995**, *128*, 209−217.

(10) Liu, C.; Karim, A. M.; Lebarbier, V. M.; Mei, D.; Wang, Y. Vapor Phase Ketonization of Acetic Acid on Ceria Based Metal Oxides. *Top. Catal.* **2013**, *56*, 1782−1789.

(11) Pestman, R.; Koster, R. M.; van Duijne, A.; Pieterse, J. A. Z.; Ponec, V. Reactions of Carboxylic Acids on Oxides: 2. Bimolecular Reaction of Aliphatic Acids to Ketones. *J. Catal.* **1997**, *168*, 265−272.

(12) Dooley, K. M.; Bhat, A. K.; Plaisance, C. P.; Roy, A. D. Ketones from Acid Condensation using Supported CeO_2 catalysts: Effect of Additives. *Appl. Catal., A* **2007**, *320*, 122−133.

(13) Snell, R. W.; Shanks, B. H. Insights into the Ceria-Catalyzed Ketonization Reaction for Biofuels Applications. *ACS Catal.* **2013**, *3*, 783−789.

(14) Calaza, F. C.; Chen, T.-L.; Mullins, D. R.; Xu, Y.; Overbury, S. H. Reactivity and Reaction Intermediates for Acetic Acid Adsorbed on CeO_2(1 1 1). *Catal. Today* **2015**, *253*, 65−76.

(15) Hakim, S. H.; Shanks, B. H.; Dumesic, J. A. Catalytic Upgrading of the Light Fraction of a Simulated Bio-Oil over $CeZrO_x$ Catalyst. *Appl. Catal., B* **2013**, *142−143*, 368−376.

(16) Nagashima, O.; Sato, S.; Takahashi, R.; Sodesawa, T. Ketonization of Carboxylic Acids over CeO_2-Based Composite Oxides. *J. Mol. Catal. A: Chem.* **2005**, *227*, 231−239.

(17) Martinez, R.; Huff, M. C.; Barteau, M. A. Ketonization of Acetic Acid on Titania-Functionalized Silica Monoliths. *J. Catal.* **2004**, *222*, 404−409.

(18) Pestman, R.; van Duijne, A.; Pieterse, J. A. Z.; Ponec, V. The Formation of Ketones and Aldehydes from Carboxylic Acids, Structure-Activity Relationship for Two Competitive Reactions. *J. Mol. Catal. A: Chem.* **1995**, *103*, 175−180.

(19) Pham, T. N.; Shi, D.; Resasco, D. E. Kinetics and Mechanism of Ketonization of Acetic Acid on Ru/TiO_2 Catalyst. *Top. Catal.* **2014**, *57*, 706−714.

(20) Pham, T. N.; Shi, D.; Resasco, D. E. Reaction Kinetics and Mechanism of Ketonization of Aliphatic Carboxylic Acids with Different Carbon Chain Lengths over Ru/TiO_2 Catalyst. *J. Catal.* **2014**, *314*, 149−158.

(21) Hasan, M. A.; Zaki, M. I.; Pasupulety, L. Oxide-Catalyzed Conversion of Acetic Acid into Acetone: An FTIR Spectroscopic Investigation. *Appl. Catal., A* **2003**, *243*, 81−92.

(22) Ignatchenko, A. V.; DeRaddo, J. S.; Marino, V. J.; Mercado, A. Cross-Selectivity in the Catalytic Ketonization of Carboxylic Acids. *Appl. Catal., A* **2015**, *498*, 10−24.

(23) Wang, S.; Iglesia, E. Experimental and Theoretical Assessment of the Mechanism and Site Requirements for Ketonization of Carboxylic Acids on Oxides. *J. Catal.* **2017**, *345*, 183−206.

(24) Pulido, A.; Oliver-Tomas, B.; Renz, M.; Boronat, M.; Corma, A. Ketonic Decarboxylation Reaction Mechanism: A Combined Experimental and DFT Study. *ChemSusChem* **2013**, *6*, 141−151.

(25) Okumura, K.; Iwasawa, Y. Zirconium Oxides Dispersed on Silica Derived from Cp_2ZrCl_2, $[(i\text{-PrCp})_2ZrH(\mu\text{-H})]_2$, and $Zr(OEt)_4$ Characterized by X-Ray Absorption Fine Structure and Catalytic Ketonization of Acetic Acid. *J. Catal.* **1996**, *164*, 440−448.

(26) Lee, Y.; Choi, J.-W.; Suh, D. J.; Ha, J.-M.; Lee, C. H. Ketonization of Hexanoic Acid to Diesel-Blendable 6-Undecanone on the Stable Zirconia Aerogel Catalyst. *Appl. Catal., A* **2015**, *506*, 288−293.

(27) Ignatchenko, A. V.; Kozliak, E. I. Distinguishing Enolic and Carbonyl Components in the Mechanism of Carboxylic Acid Ketonization on Monoclinic Zirconia. *ACS Catal.* **2012**, *2*, 1555−1562.

(28) Tosoni, S.; Pacchioni, G. Acetic Acid Ketonization on Tetragonal Zirconia: Role of Surface Reduction. *J. Catal.* **2016**, *344*, 465−473.

(29) Gines, M. J. L.; Iglesia, E. Bifunctional Condensation Reactions of Alcohols on Basic Oxides Modified by Copper and Potassium. *J. Catal.* **1998**, *176*, 155−172.

(30) Wang, S.; Goulas, K.; Iglesia, E. Condensation and Esterification Reactions of Alkanals, Alkanones, and Alkanols on TiO_2: Elementary Steps, Site Requirements, and Synergistic Effects of Bifunctional Strategies. *J. Catal.* **2016**, *340*, 302−320.

(31) Wang, S.; Iglesia, E. Substituent Effects and Molecular Descriptors of Reactivity in Condensation and Esterification Reactions of Oxygenates on Acid−Base Pairs at TiO_2 and ZrO_2 Surfaces. *J. Phys. Chem. C* **2016**, *120*, 21589−21616.

(32) Li, W.; Huang, H.; Li, H.; Zhang, W.; Liu, H. Facile Synthesis of Pure Monoclinic and Tetragonal Zirconia Nanoparticles and Their Phase Effects on the Behavior of Supported Molybdena Catalysts for Methanol-Selective Oxidation. *Langmuir* **2008**, *24*, 8358−8366.

(33) Xie, S.; Iglesia, E.; Bell, A. T. Water-Assisted Tetragonal-to-Monoclinic Phase Transformation of ZrO_2 at Low Temperatures. *Chem. Mater.* **2000**, *12*, 2442−2447.

(34) Kresse, G.; Furthmuller, J. Efficiency of *Ab-Initio* Total Energy Calculations for Metals and Semiconductors using a Plane-Wave Basis Set. *Comput. Mater. Sci.* **1996**, *6*, 15−50.

(35) Kresse, G.; Furthmuller, J. Efficient Iterative Schemes for *Ab Initio* Total-Energy Calculations using a Plane-Wave Basis Set. *Phys. Rev. B: Condens. Matter Mater. Phys.* **1996**, *54*, 11169−11186.

(36) Kresse, G.; Hafner, J. *Ab Initio* Molecular Dynamics for Liquid Metals. *Phys. Rev. B: Condens. Matter Mater. Phys.* **1993**, *47*, 558−561.

(37) Kresse, G.; Hafner, J. *Ab Initio* Molecular-Dynamics Simulation of the Liquid-Metal-Amorphous-Semiconductor Transition in Germanium. *Phys. Rev. B: Condens. Matter Mater. Phys.* **1994**, *49*, 14251−14269.

(38) Blöchl, P. E. Projector Augmented-Wave Method. *Phys. Rev. B: Condens. Matter Mater. Phys.* **1994**, *50*, 17953−17979.

(39) Kresse, G.; Joubert, D. From Ultrasoft Pseudopotentials to the Projector Augmented-Wave Method. *Phys. Rev. B: Condens. Matter Mater. Phys.* **1999**, *59*, 1758−1775.

(40) Perdew, J. P.; Burke, K.; Ernzerhof, M. Generalized Gradient Approximation Made Simple. *Phys. Rev. Lett.* **1996**, *77*, 3865−3868.

(41) Perdew, J. P.; Burke, K.; Ernzerhof, M. Generalized Gradient Approximation Made Simple [Phys. Rev. Lett. 77, 3865 (1996)]. *Phys. Rev. Lett.* **1997**, *78*, 1396.

(42) Wu, X.; Vargas, M. C.; Nayak, S.; Lotrich, V.; Scoles, G. Towards Extending the Applicability of Density Functional Theory to Weakly Bound Systems. *J. Chem. Phys.* **2001**, *115*, 8748−8757.

(43) Grimme, S.; Ehrlich, S.; Goerigk, L. Effect of the Damping Function in Dispersion Corrected Density Functional Theory. *J. Comput. Chem.* **2011**, *32*, 1456−1465.

(44) Monkhorst, H. J.; Pack, J. D. Special Points for Brillouin-Zone Integrations. *Phys. Rev. B* **1976**, *13*, 5188−5192.

(45) Makov, G.; Payne, M. C. Periodic Boundary Conditions in *Ab Initio* Calculations. *Phys. Rev. B: Condens. Matter Mater. Phys.* **1995**, *51*, 4014−4022.

(46) Henkelman, G.; Jonsson, H. A. Improved Tangent Estimate in the Nudged Elastic Band Method for Finding Minimum Energy Paths and Saddle Points. *J. Chem. Phys.* **2000**, *113*, 9978−9985.

(47) Jonsson, H. A.; Mills, G.; Jacobsen, K. W. *Nudged Elastic Band Method for Finding Minimum Energy Paths of Transitions*; World Scientific, 1998.

(48) Henkelman, G.; Jonsson, H. A. A Dimer Method for Finding Saddle Points on High Dimensional Potential Surfaces using only First Derivatives. *J. Chem. Phys.* **1999**, *111*, 7010−7022.

(49) McQuarrie, D. A. *Statistical Mechanics*; University Science Books: Sausalito, CA, 2000.

(50) Deshlahra, P.; Iglesia, E. Methanol Oxidative Dehydrogenation on Oxide Catalysts: Molecular and Dissociative Routes and Hydrogen Addition Energies as Descriptors of Reactivity. *J. Phys. Chem. C* **2014**, *118*, 26115−26129.

(51) Campbell, C. T.; Sellers, J. R. V. Enthalpies and Entropies of Adsorption on Well-Defined Oxide Surfaces: Experimental Measurements. *Chem. Rev.* **2013**, *113*, 4106−4135.

(52) Herrmann, S.; Iglesia, E. Elementary Steps in Acetone Condensation Reactions Catalyzed by Aluminosilicates with Diverse Void Structures. *J. Catal.* **2017**, *346*, 134−153.

(53) Köck, E.-M.; Kogler, M.; Bielz, T.; Klötzer, B.; Penner, S. In situ FT-IR Spectroscopic Study of CO_2 and CO Adsorption on Y_2O_3, ZrO_2, and Yttria-Stabilized ZrO_2. *J. Phys. Chem. C* **2013**, *117*, 17666−17673.

(54) Liao, L.-F.; Lien, C.-F.; Lin, J.-L. FTIR Study of Adsorption and Photoreactions of Acetic Acid on TiO_2. *Phys. Chem. Chem. Phys.* **2001**, *3*, 3831−3837.